Performance comparison of planar, tubular and Delta8 solid oxide fuel cells using a generalized finite volume model

Florian P. Nagel, Tilman J. Schildhauer*, Serge M.A. Biollaz, Alexander Wokaun

Paul Scherrer Institut, Laboratory for Energy and Materials Cycles, Department General Energy, CH-5232 Villigen PSI, Switzerland

A B S T R A C T

A generalized, finite volume-based SOFC model is presented which includes charge, mass and heat transport as well as a Langmuir–Hinshelwood type applied kinetic model for steam reforming reactions. The model development aimed at fast applicability to various cell geometries, short calculation times to allow for system analysis calculations and high fuel flexibility. In the first part of the paper, the model approach and assumptions are presented in detail. In the second part, the generalized model is applied to a planar, the standard tubular and the triangular tube cell geometry. The validation against experimental and benchmark test data is stressed to assure comparability of the model results for the three investigated cell designs. In the last part, the three cell designs are compared, highlighting the differences with respect to internal heat- and mass transfer and the impact on the electrochemical performance. It is shown that the performance of the triangular tube cell is almost double that of the standard tubular cell designs. The planar cell is outperformed by the triangular tube cell as well.

© 2008 Elsevier B.V. All rights reserved.

1. Introduction

Solid oxide fuel cells (SOFC) feature high efficiency in converting gaseous fuels to electricity at scales ranging from kilowatts to megawatts. Hydrogen and carbon monoxide are fuels for SOFCs and the operational temperatures departing between 700 °C and 1000 °C enable the indirect conversion of hydrocarbons via steam reforming reactions. Recently, evidence for direct conversion of hydrocarbons was found [1]. For this reason SOFCs have widely been considered as the most fuel-flexible fuel cell type. Besides, the high exhaust temperatures predestine SOFCs for the combination with gas turbines (GT). Such SOFC/GT systems are expected to reach electrical efficiencies up to 65% [2].

SOFC development is still in progress and a number of cell designs with specific advantages and drawbacks are under investigation. The most important cell designs are the planar and the tubular designs. Planar SOFCs feature short current paths resulting in low electrical resistance and high power densities. However, planar cells suffer from thermal stress resulting from different thermal expansion coefficients of the employed materials for the anode–electrolyte–cathode (AEC) assemblies, the interconnector plates (IC) and the sealings. Tubular cells have considerably less problems with thermal stress and are therefore very robust. Long-

duration tests with tubular cells up to 69,000 h were reported [3]. The seal-less tubular cell design involves however long current paths and higher electrical resistance than planar cells. The current path length further limits the size of tubular cells which complicates a cost-effective production. The triangular tube cell, in the following referred to as Delta8 cell, combines the advantages of the seal-less design with shortened current paths and larger cell sizes which result in lower production cost.

From the mentioned differences of these three cell designs, the question arises what the impact of the specific cell design characteristics on the overall system is. This point is even more important, when non-standard fuels such as producer gases containing tars and hydrocarbons shall be applied. Purely experimental investigations are hardly applicable to solve this issue due to the high costs involved. Therefore, numerical modeling of SOFCs has drawn a lot of interest in the past years.

Usually simplified models have been employed for systems analysis calculations, concentrating on the overall cell performance, e.g. [4–8]. This approach is valid at standard operating conditions; however it is questionable for the prediction at non-standard operating conditions such as e.g. operation with other fuels or electrical loads. For such investigations, more complex models are required which consider the internal charge, heat and mass transfer processes locally resolved instead of averaged over the entire cell.

Typically computational fluid dynamics (CFD) codes have been employed for cell design optimization. The calculation times of 25–50 min [9], however, hindering an application of CFD-based

* Corresponding author. Tel.: +41 56 310 27 06; fax: +41 56 310 21 99.
  E-mail address: tilman.schildhauer@psi.ch (T.J. Schildhauer).

Nomenclature

A	area (m^2)
AEC	anode–electrolyte–cathode assembly
c_p	heat capacity ($J\,mol^{-1}\,K^{-1}$)
CV	control volume
d	diameter (m)
D	diffusion coefficient ($m^2\,s^{-1}$)
D_K	Knudsen diffusion coefficient ($m^2\,s^{-1}$)
D_m	molecular diffusion coefficient ($m^2\,s^{-1}$)
E	voltage (V)
E_{act}	activation energy for exchange current density calculation ($J\,mol^{-1}$)
Eq_{H_2}	hydrogen equivalent molar flow ($mol\,s^{-1}$)
F	Faraday constant ($C\,mol^{-1}$)
h	height of gas channel, bipolar plate, etc. (m)
I	current density ($A\,m^{-2}$)
I_0	exchange current density ($A\,m^{-2}$)
K_p	equilibrium constant
l	length (m)
l_c	length of planar cell (m)
l_{D8}	length of Delta8 cell (m)
l_t	length of tubular cell (m)
L	length of cell-subunit (m)
LHV	lower heating value ($J\,mol^{-1}$)
M	molecular weight ($kg\,mol^{-1}$)
n	number of exchanged electrons per electrochem. reaction
n_{ch}	number of channels of planar cell
n_{dot}	molar flow ($mol\,s^{-1}$)
n_{RE}	number of repeating elements
n_{tri}	number of triangular tubes forming the Delta8 cell
Nu	Nusselt number
p	total or partial pressure ($N\,m^{-2}$)
P_{el}	electrical power (DC) (W)
Q_{dot}	heat flux ($W\,m^{-1}$)
r	radius (m)
r_j	reaction rate of reaction j [$mol\,s^{-1}\,m^{-1}$]
$r_{dl-reac}$	diff. limited and integration length specific reaction rate ($mol\,s^{-1}\,m^{-1}$)
r_i	inner radius (m)
r_m	middle radius (m)
r_o	outer radius (m)
ro	reaction order
R	resistance (Ω); ideal gas constant ($J\,mol^{-1}\,K^{-1}$)
T	temperature (K)
T_{adtK}	gas temperature in air delivery tube (K)
T_{aK}	anode gas temperature (K)
T_{amb}	ambient temperature (K)
T_{sK}	solid structure temperature (K)
UF	fuel utilization
w_c	channel width of planar cell channels (m)
w_{ce}	width of planar cell (m)
w_{D8}	Delta8 cell width (m)
x_p	active fraction of planar cell area covered by bipolar rib
x_t	inactive fraction of tubular cell area
y	molar fraction

Greek letters

α	upper triangular half angle (°)
α_{an}	convective heat exchange coefficient at anode ($W\,m^{-2}\,K^{-1}$)
α_{ca}	convective heat exchange coefficient at cathode ($W\,m^{-2}\,K^{-1}$)
α_{insul}	heat transfer coefficient through insulation ($W\,m^{-2}\,K^{-1}$)
β	transfer coefficient
$\beta_{x,diff}$	mass transfer coefficient of specie x ($m\,s^{-1}$)
$\beta_{x,diff-reac}$	diff. limited reaction conversion coefficient of specie x
$\beta_{x,reac}$	reaction conversion coefficient of specie x
δ	thickness of component, Delta8 cell wall thickness (m)
ΔH	heat of reaction ($J\,mol^{-1}$)
ε	porosity of porous media
γ	pre-exponential factor for exchange current density ($A\,m^{-2}$)
η_{act}	activation polarization voltage loss (V)
η_{diff}	diffusion polarization voltage loss (V)
η_{ohm}	ohmic voltage loss (V)
λ	air-to-fuel ratio
λ_s	solid structure heat conductivity coefficient ($W\,m^{-1}\,K^{-1}$)
λ_{an}	thermal conductivity of anode gas ($W\,m^{-1}\,K^{-1}$)
λ_{ca}	thermal conductivity of cathode gas ($W\,m^{-1}\,K^{-1}$)
ν_{av}	average molecular speed ($m\,s^{-1}$)
ν_{ij}	stoiciometric coefficient of specie i in reaction j
ρ	specific conductivity ($1\,\Omega^{-1}\,m^{-1}$)
τ	tortuosity of porous media

Subscripts and superscripts

0, in	inlet
act	active
ADT	air delivery tube
AEC	anode–electrolyte–cathode assembly
an	anode gas channel, anode electrode
av	average
ca	cathode gas channel, cathode electrode
chact	chemically active
circ	circumferential
conv	convective
cross	cross-sectional
cs	catalyst surface
D8	Delta8
ed	educts
eff	effective
el	electrolyte
elact	electrochemically active
equiv	equivalent
FC	fuel cell tube
hloss	heat loss
hyd	hydraulic
ic	interconnect
ion	ionization
mix	gas mixture
op	operational
oxi	oxidation
p	planar
prod	products
SH	sensible heat
stoic	stoiciometric
STR	steam reforming
t	tubular
tot	total
TPB	triple phase boundary
WGS	water–gas-shift

models in systems analysis calculations which often require several hundred iterative steps to find an overall solution for the investigated system. Further, CFD models require an exact description of the cell geometry and the definition of the calculation mesh, both being time consuming tasks.

We propose a generalized model that allows for the fast application to diverse cell designs, considers all important internal processes and at the same time features short calculation times of approximately 2 min enabling overall system simulations.

2. Model definition

Our model computes temperature, reactant partial pressure, current density and voltage loss distributions. In addition, integral values such as the absolute power output, fuel and air utilization are predicted for a user-defined operational voltage, fuel and air input flow and temperature. Any combination of H_2, CO, CO_2, H_2O, CH_4 and N_2 is allowed as fuel composition and the oxygen fraction in the cathode gas can be set to any value. The electrochemical conversion of hydrogen and carbon monoxide are considered to occur in parallel. Methane oxidation through reforming reactions is also considered via a Langmuir–Hinshelwood kinetic model.

2.1. Assumptions, definitions and model structure

The main assumptions of our model are:

- Steady-state conditions are assumed.
- The considered SOFC can be axially divided into a number of continuously stirred tank reactors (CSTR), termed control volumes (CV).
- Pressure losses in the gas channels are not considered.
- Due to their high electrical conductivity, the interconnector or bipolar plates of planar cell designs are considered equipotential [10].
- The flow regime in the gas channels is assumed as plug flow [11]. Turbulent flow is not considered, despite its possible occurrence in the oxidant gas channels due to excessive flows of cooling air [12]. Mass transport in normal direction to the flow direction is assumed to be by diffusion only.
- A constant Nusselt number with the value 4 is assumed [11].
- Radiative heat transport between solid structures and gas streams is ignored [12].
- The heats of heterogeneous reactions are attributed to the fuel cell solid structure.
- The diffusion of reactants through the gas channel to the catalytic surface is considered.
- The water–gas-shift reaction is regarded as a homogenous reaction at equilibrium. This assumption is found very frequently in the literature, e.g. [10,13,14], and was confirmed in experiments conducted by the authors (manuscript in preparation).

Besides local values such as solid temperature and current density, our model calculates integral values which characterize the operational conditions of the investigated cell design and fuel composition. The definitions are given in the following:

- The fuel utilization is defined as the ratio of the hydrogen equivalent mol flows at the cell inlet and outlet.

$$\text{UF} = 1 - \frac{Eq_{H_2,\text{out}}}{Eq_{H_2,\text{in}}} \quad \text{with} \quad Eq_{H_2} = y_{H_2} + y_{CO} + 4y_{CH_4} \tag{1}$$

The hydrogen equivalent mol flow, Eq_{H_2}, is calculated assuming that all methane is completely reformed to hydrogen and carbon dioxide.

Our model consists of three coupled sub-models, namely the electrochemical performance model, the mass balance model and the energy balance model. Fig. 1 depicts the model structure and the iterative solution algorithm. The three sub-models are coupled via the fuel composition and the temperatures of the gases and the solid structure yielding a highly non-linear equation system which can only be solved iteratively. In this work, the modeling package "ATHENA Visual Studio 11.0" [15], was used to implement the numerical code in the FORTRAN language.

The electrochemical performance model calculates the current density for a given fuel composition and operational voltage in a control volume. The core of the model is the voltage balance according to which the Nernst voltage minus the current density-dependent voltage losses has to equal the operational voltage.

The mass balance model requires the current density as input for the calculation of the conversion rates of the electrochemically active species. According to the aforementioned assumptions, these are hydrogen and carbon monoxide. Furthermore, the mass balance model includes the calculation of reaction rates for all considered homogenous and heterogeneous reactions. Besides, the mass balance model calculates the heat source terms and the convective heat transport terms, which are coupled to the reactant transport to and from the electrode surfaces.

The energy balance model serves for the calculation of the effective temperatures of the solid structure and the gas channels based on the heat source terms stemming from the mass balance model. Furthermore, the energy balance model includes the calculation of the purely convective heat transfer between the gases and the solid structure as well as the conductive heat transport within the solid structure.

2.2. Gas and solid material properties

2.2.1. Thermodynamic properties of gases

The calculation of the thermodynamic properties of the involved species is the basis of any numerical model of a technical process or apparatus. The mean temperature and the temperature variation occurring in the process determines the which correlations are the most suitable. For processes which are operated in a narrow temperature band it is valid to assume temperature independent material properties. This approach is not applicable to fuel cell models due to the fuel cell operational temperatures which can vary from 700 °C to 1000 °C, see [16].

For the estimation of the heat capacity, thermal conductivity and viscosity of pure gas species, correlations according to the DIPPR 801 standard (Design Institute for Physical Property Data) were implemented as subroutines [17,18]. In order to enable the prediction of diffusion limited phenomena, our model includes a subroutine for the calculation of effective diffusion coefficients. Two cases were considered to describe the diffusion of gases through the electrodes of fuel cells. The first case is the Knudsen diffusion, which is of importance when the mean free path length of the gas molecules is large, compared to the pore diameter. In this case, the molecules collide more often with the pore walls then with each other. The corresponding Knudsen diffusion coefficient is calculated according to:

$$D_{K,x} = \frac{2}{3} r_{\text{pore}} v_{\text{av},x} \quad \text{with} \quad v_{\text{av},x} = \left(\frac{8RT}{\pi M_i}\right)^{0.5} \tag{2}$$

The second case is the molecular diffusion, where the mean free path length of the molecules is small compared to the pore diameter. In this case, the gas molecules collide more frequently with each other than with the pore walls. For the calculation of the molecular diffusion coefficients the method according to the kinetic gas theory and the Fuller method were implemented. Detailed information
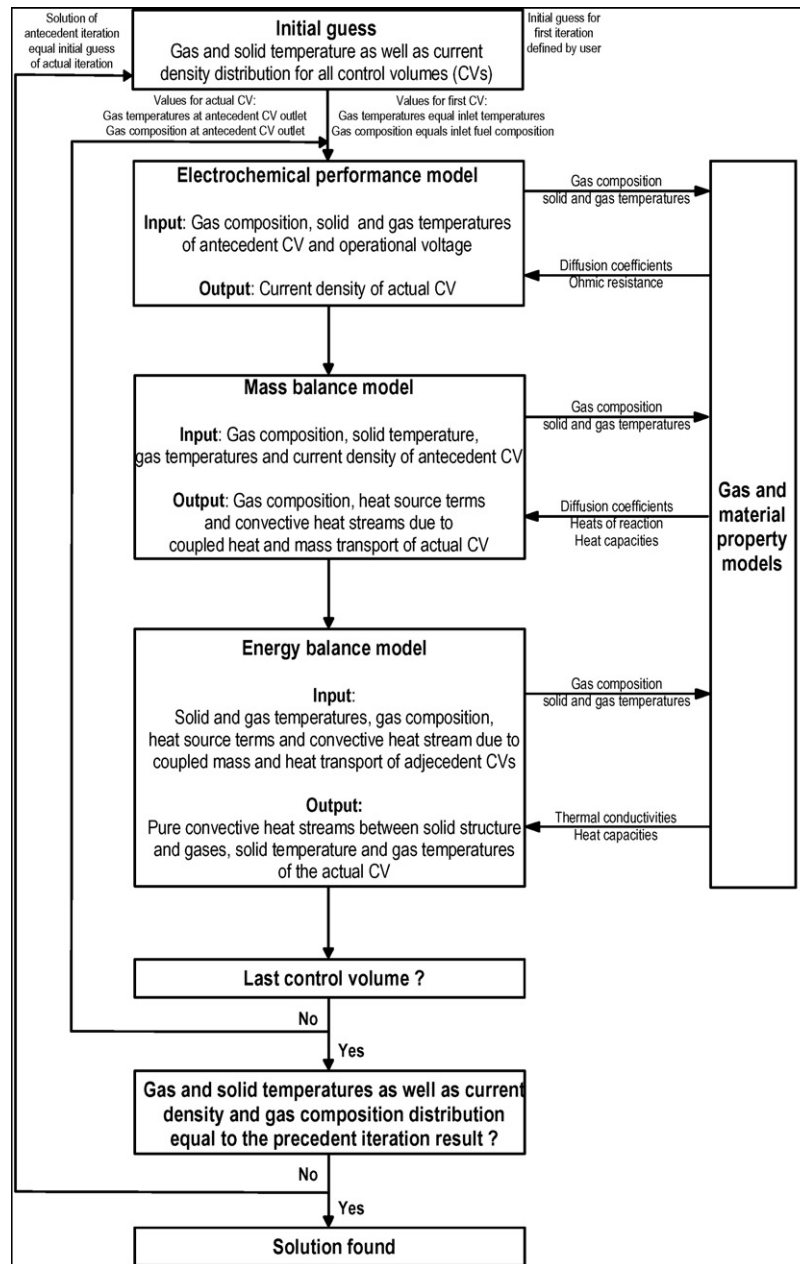
Fig. 1. Model structure and iterative solution algorithm.

about both methods can be found in [19]. In order to estimate the molecular diffusion coefficient of a specific species in gas mixtures, the following mixing rule was implemented [19]:

$$D_{m,\mathrm{mix},x} = \frac{1 - y_x}{\sum\limits_i y_i / D_{\mathrm{m},i,x}} \qquad (3)$$

2.2.2. Temperature-dependent solid material properties

The materials used in solid oxide fuel cells have to fulfill different tasks and their physical properties influence the behavior of the cell. The most important properties in this respect are the electrical and the ionic conductivities, which have a direct influence on the power output of the cell. As a general rule, the ceramic materials employed in SOFCs have only poor electrical and ionic conductivities at room temperatures. At elevated temperatures however the

conductivity improves. The employed correlations for the temperature dependent specific conductivity were proposed in [12]:

$$\rho_{\mathrm{an}} = \frac{95.0 \times 10^6}{T_{\mathrm{sK}}} \exp\left(\frac{-1150.0}{T_{\mathrm{sK}}}\right) \qquad (4)$$

$$\rho_{\mathrm{el}} = 3.34 \times 10^4 \exp\left(\frac{10300.0}{T_{\mathrm{sK}}}\right) \qquad (5)$$

$$\rho_{\mathrm{ca}} = \frac{42.0 \times 10^6}{T_{\mathrm{sK}}} \exp\left(\frac{-1200.0}{T_{\mathrm{sK}}}\right) \qquad (6)$$

$$\rho_{\mathrm{ic}} = \frac{9.3 \times 10^6}{T_{\mathrm{sK}}} \exp\left(\frac{-1100.0}{T_{\mathrm{sK}}}\right) \qquad (7)$$

2.3. Geometries and discretization

Fuel cell designs under development mainly differ in the geometry and the employed materials. Concerning the geometry, it is very useful to distinguish between the macro- and the microgeometry of fuel cells. The micro geometry describes the construction of the AEC assembly, while the macrogeometry describes the construction of the cell itself.

The micro geometry has a strong influence on the electrochemical performance of the fuel cell via ohmic losses and transport limitations due to the diffusion of the reacting species through the electrodes to the sites where the electrochemical reactions occur.

The macrogeometry has an impact on the electrochemical performance via ohmic losses occurring in the current conducting components of the fuel cell, the heat balance via convective and conductive heat exchange areas and the mass balance via the catalytically active surfaces areas.

Accounting for the strong influence of the micro- and macrogeometries of different fuel cell designs on the cell characteristics was the most important requirement for our model. The chosen approach for describing the geometry is based on characteristic lengths and areas. The corresponding definitions for the considered geometries are presented in the following.

2.3.1. Planar geometry

Fig. 2 depicts the considered planar geometry. The planar cell stack consists of bipolar plates which form the rectangular gas channels. The bipolar plates are separated by AEC assemblies. The surface of the AEC assemblies is consequently partially covered by the ribs of the bipolar plates. The planar cell is divided into repeating structures according to the number of gas channels. The following characteristic lengths and areas were defined for the repeating structure of the planar geometry:

- Total active area, $A_{p,act}$

$$A_{p,act} = \left(\frac{w_{ce}}{n_{ch}} \right) l_c \tag{8}$$

- Electrochemically active length, $l_{p,elact}$

$$l_{p,elact} = w_c + \left(\left(\frac{w_{ce}}{n_{ch}} \right) - w_c \right) x_{p,elact} \tag{9}$$

- Chemically active length, $l_{p,chact}$

$$l_{p,chact} = w_c + \left(\left(\frac{w_{ce}}{n_{ch}} \right) - w_c \right) x_{p,chact} \tag{10}$$

- Hydraulic diameter of anode gas channel, $d_{p,hyd,an}$

$$d_{p,hyd,an} = \frac{2w_c h_{p,an}}{w_c + h_{p,an}} \tag{11}$$

- Hydraulic diameter of cathode gas channel, $d_{p,hyd,ca}$

$$d_{p,hyd,ca} = \frac{2w_c h_{p,ca}}{w_c + h_{p,ca}} \tag{12}$$

- Circumferential length of anode channel perpendicular to gas flow, $l_{p,circ,an}$

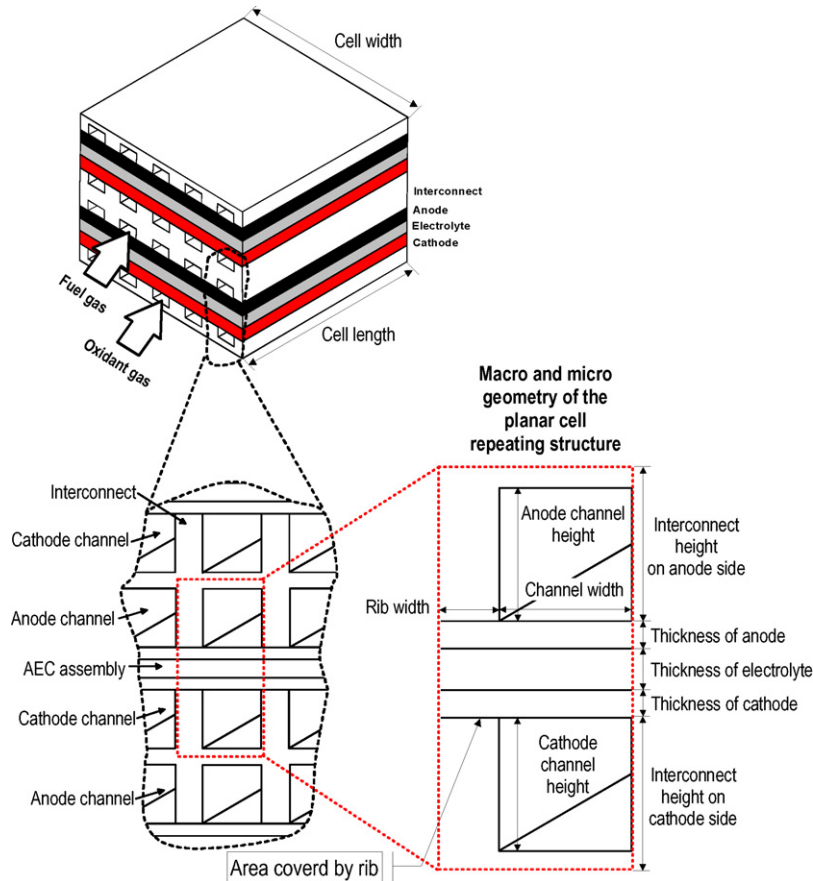$$l_{p,circ,an} = 2(w_c + h_{p,an}) \tag{13}$$

Fig. 2. Generalized planar cell geometry and repeating structure description.
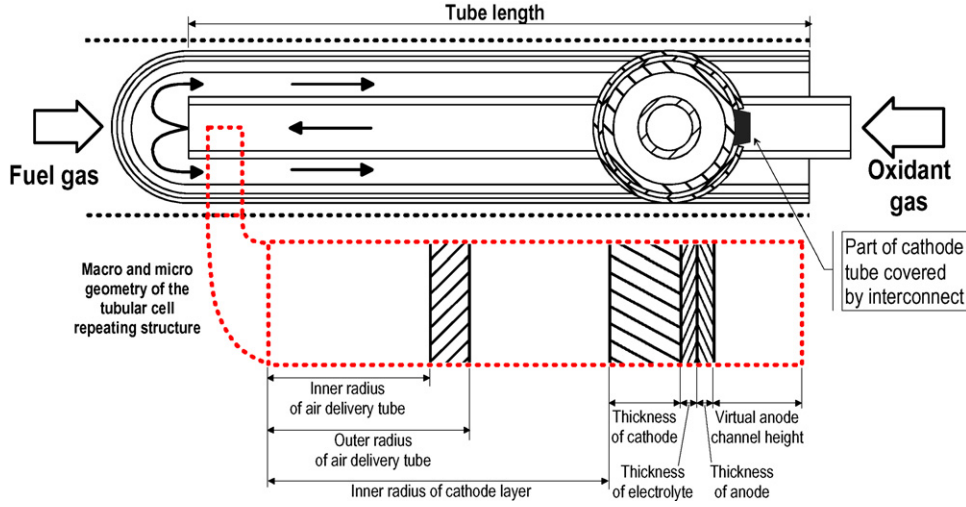
Fig. 3. Standard tubular cell geometry.

- Circumferential length of cathode channel perpendicular to gas flow, $l_{p,circ,ca}$

$$l_{p,circ,ca} = 2(w_c + h_{p,ca}) \tag{14}$$

- Cross-sectional area of solid structure perpendicular to gas flow direction, $A_{p,cross}$

$$A_{p,cross} = \left(\frac{w_{ce}}{n_{ch}}\right)(h_{ic,an} + \delta_{p,an} + \delta_{p,el} + \delta_{p,ca} + h_{ic,ca})$$
$$-w_c(h_{p,an} + h_{p,ca}) \tag{15}$$

2.3.2. Tubular geometry

Fig. 3 depicts the standard tubular geometry. The standard tubular cell consists of a AEC tube with one closed end and a concentric air delivery tube (ADT). The annular gap between the outer surface of the ADT and inner surface of the AEC tube forms the cathode gas channel. The anode gas flows around the outer surface of the tube. Thus, the geometry of the anode gas channel is not defined by the cell design itself but rather by the arrangement of the single tubes in the stack. For modeling purposes however, an annular gap shaped anode gas channel was assumed. The fuel cell tube itself was considered as a repeating structure. The following characteristic lengths and areas were defined for the tubular geometry:

- Middle radius of the AEC assembly, $r_{m,AEC}$

$$r_{m,AEC} = \frac{r_{i,FC} + (\delta_{t,ca} + \delta_{t,el} + \delta_{t,an})}{2} \tag{16}$$

- Outer radius of the cell tube, $r_{o,FC}$

$$r_{o,FC} = r_{i,FC} + \delta_{t,ca} + \delta_{t,el} + \delta_{t,an} \tag{17}$$

- Total active area, $A_{t,act}$

$$A_{t,act} = 2\pi r_{m,AEC} l_t \tag{18}$$

- Electrochemically active circumferential length, $l_{t,elact}$

$$l_{t,elact} = 2\pi r_{m,AEC}(1 - x_{t,ic}) \tag{19}$$

- Chemically active circumferential length, $l_{t,chact}$

$$l_{t,chact} = 2\pi r_{o,FC}(1 - x_{t,ic}) \tag{20}$$

- Hydraulic diameter of air delivery tube, $d_{t,hyd,ADT}$

$$d_{t,hyd,ADT} = 2r_{i,ADT} \tag{21}$$

- Hydraulic diameter of virtual anode gas channel, $d_{t,hyd,an}$

$$d_{t,hyd,an} = 2 \cdot h_{t,an} \tag{22}$$

- Hydraulic diameter of cathode gas channel, $d_{t,hyd,ca}$

$$d_{t,hyd,ca} = 2(r_{i,FC} - r_{o,ADT}) \tag{23}$$

- Circumferential length of air delivery tube perpendicular to gas flow, $l_{t,circ,ADT}$

$$l_{t,circ,ADT} = \pi(r_{o,ADT} + r_{i,ADT}) \tag{24}$$

- Circumferential length of virtual anode channel perpendicular to gas flow, $l_{t,circ,an}$

$$l_{t,circ,an} = 2\pi r_{o,FC}(1 - x_{t,ic}) \tag{25}$$

- Circumferential length of cathode channel perpendicular to gas flow, $l_{t,circ,ca}$

$$l_{t,circ,ca} = 2\pi r_{i,FC} \tag{26}$$

- Cross-sectional area of solid structure perpendicular to gas flow direction, $A_{t,cross}$

$$A_{t,cross} = (\pi r_{o,FC}^2) - (\pi r_{i,FC}^2) \tag{27}$$

2.3.3. Triangular tube geometry

Fig. 4 depicts the triangular tube geometry (D8). It is assumed that similar to the standard tubular cells, the D8 employs centered air delivery tubes (ADT) for the injection of the cathode air. The D8 cell is made up of eight connected triangular-shaped AEC tubes with triangular cross-section and closed ends, Fig. 4a. The spaces between the ADTs and inner surfaces of the triangular AEC tubes form the cathode gas channels, Fig. 4d. The outer upper surface of the D8 cell and the outer lower surface of the next D8 cell form the anode gas channels, Fig. 4d. Note that the D8 cells are stacked like planar cells, Fig. 4a. For better contacting and current distribution, a porous contact layer is placed between the individual cells. Due to its high electrical conductivity and porosity, the contact layer was not considered in our model. The D8 repeating structure was defined as one triangular-shaped AEC tube.

The description of the triangular cell design macro geometry is more complex than that of the standard tubular and planar cell design. However, the complexity can be reduced by introducing geometrical dependencies for the curvature radii. For our model, it was assumed that the upper outer curvature radius r_o equals
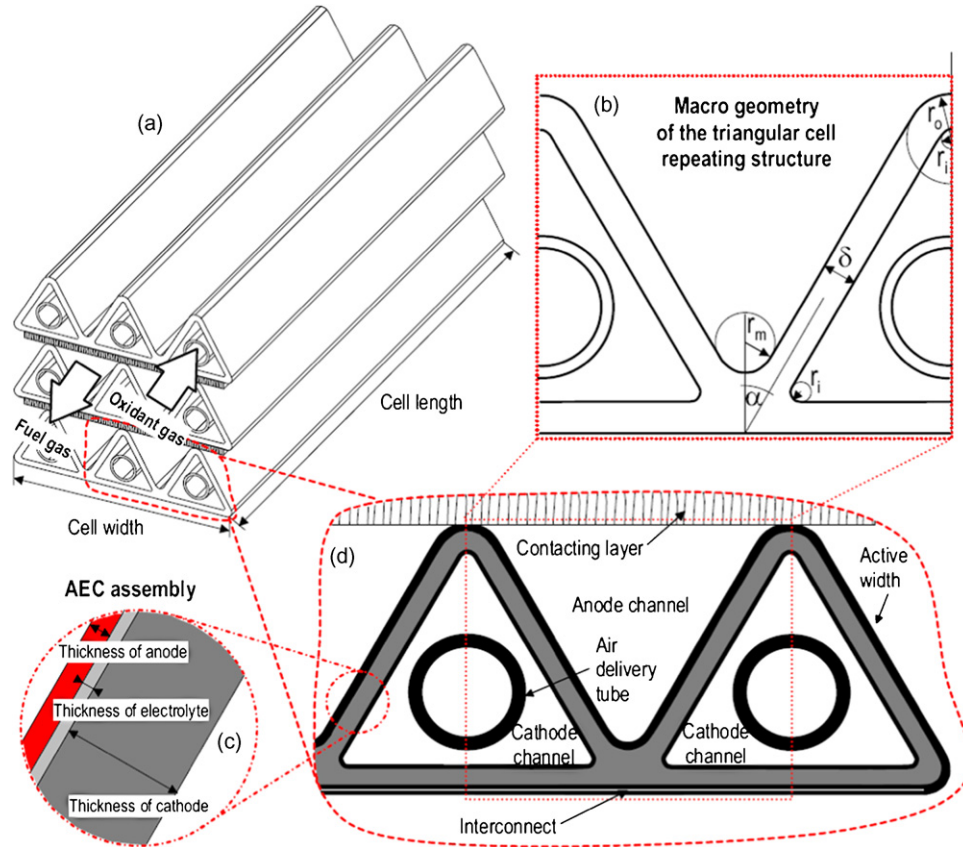
Fig. 4. Triangular tube cell geometry.

1.5 times the D8 cell tube wall thickness δ. The lower outer curvature radius r_m was assumed equal to the cell tube wall thickness and the inner curvature radius r_i equal to half the cell tube wall thickness, Fig. 4b. With the mentioned assumptions the following characteristic lengths and areas were derived for the triangular geometry:

- Electrochemically and chemically active width, $l_{D8,elact}$

$$l_{D8,\,elact} = l_{D8,\,chact} = \frac{2\delta}{n_{tri}\cos\alpha} + \frac{90-\alpha}{n_{tri}90}\pi\delta + 2X \quad \text{with}$$

$$X = \frac{w_{D8}}{n_{tri}} - \frac{5}{2}\frac{\delta}{\tan\alpha} + \frac{90-\alpha}{72}\pi\delta \tag{28}$$

The active width of one repeat element is the arithmetic average of the overall active width of the D8 cell. Note that the additional electrochemically active areas of the lower curvature of the two outer triangular cells were hence considered, Fig. 4d.

- Total active area, $A_{D8,act}$

$$A_{D8,act} = l_{D8,elact}l_{D8} \tag{29}$$

- Circumferential length of ADT perpendicular to gas flow, $l_{D8,circ,ADT}$

$$l_{D8,circ,ADT} = \pi(r_{D8,o,ADT} + r_{D8,i,ADT}) \tag{30}$$

- Circumferential length of anode channel perpendicular to gas flow, $l_{D8,circ,an}$

$$l_{D8,circ,an} = l_{D8,elact} + \frac{w_{D8}}{n_{tri}} \tag{31}$$

- Circumferential length of cathode channel perpendicular to gas flow, $l_{D8,circ,ca}$

$$l_{D8,circ,ca} = \frac{\sin\alpha + 1}{\sin\alpha}\left(\frac{w_{D8}}{n_{tri}} - \frac{\delta + 2\sin\alpha}{\cos\alpha}\right)$$

$$+ \frac{90+\alpha}{120}\pi\delta - \frac{3\delta}{\tan\left(45 - \frac{\alpha}{2}\right)} \tag{32}$$

- Cross-sectional area of cathode channel, $A_{D8,cross,ca}$

$$A_{D8,cross,ca} = \frac{X^2}{4\tan\alpha} + \frac{3}{4}\delta^2\left(\frac{90+\alpha}{360}\pi - \cot\left(45 - \frac{\alpha}{2}\right)\right)$$

$$- \pi r_{D8,o,ADT}^2 \quad \text{with} \ X = \left(\frac{w_{D8}}{n_{tri}} - \frac{\delta + 2\sin\alpha}{\cos\alpha}\right) \tag{33}$$

- Cross-sectional area of anode channel, $A_{D8,cross,an}$

$$A_{D8,cross,an} = X^2\tan\alpha + Y\frac{9}{4}\delta^2 - \frac{5}{4}\pi\delta^2\frac{90-\alpha}{180} - \frac{\delta^2}{\tan\alpha} \quad \text{with}$$

$$X = \frac{w_{D8}\cos\alpha + n_{tri}\delta(\sin\alpha - 2)}{2n_{tri}\sin\alpha} \quad \text{and}$$

$$Y = \frac{2\sin\alpha + \cos\alpha - 1 - \sin^2\alpha}{\sin\alpha\cos\alpha} \tag{34}$$

- Cross-sectional area of solid structure, $A_{D8,cross}$

$$A_{D8,cross} = \frac{w_{D8}}{n_{tri}}X - A_{D8,cross,ca} - A_{D8,cross,an} - \pi r_{D8,o,ADT}^2 \quad \text{with}$$

$$X = \left(\frac{w_{D8}\cos\alpha}{2n_{tri}\sin\alpha} - \frac{\delta}{\sin\alpha} + \frac{3}{2}\delta\right) \tag{35}$$
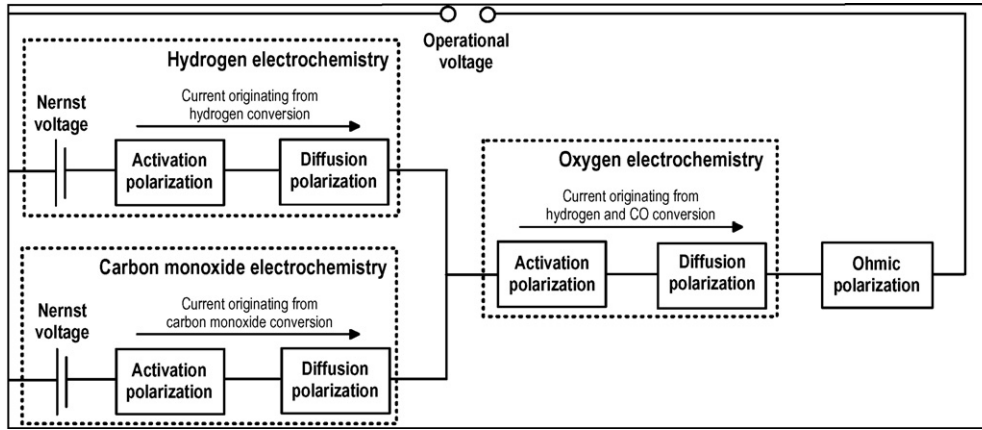
Fig. 5. Equivalent circuit of the electrochemical performance model.

- Hydraulic diameter of ADT, $d_{D8,hyd,ADT}$

$$d_{D8,\,hyd,\,ADT} = 2r_{D8,\,i,\,ADT} \tag{36}$$

- Hydraulic diameter of anode gas channel, $d_{D8,hyd,an}$

$$d_{D8,\,hyd,\,an} = \frac{4A_{D8,cross,an}}{l_{D8,cric,an}} \tag{37}$$

- Hydraulic diameter of cathode gas channel, $d_{D8,hyd,ca}$

$$d_{D8,\,hyd,\,ca} = \frac{4A_{D8,cross,ca}}{l_{D8,cric,an} + 2\pi r_{D8,i,ADT}} \tag{38}$$

2.4. Electrochemical performance model

The electrochemical performance model calculates the current density for a given fuel composition and operational voltage considering activation, ohmic and diffusion losses. Fig. 5 shows the equivalent circuit of the electrochemical performance model.

The starting point for the calculation of the current density is the reversible potential of the fuel gas, referred to as the Nernst voltage. The Nernst voltage of the hydrogen oxidation, E_{Nernst,H_2}, and carbon monoxide oxidation, $E_{Nernst,CO}$, is calculated using Eq. (39), where n stands for the number of exchanged electrons per reaction. For the oxidation of hydrogen or carbon monoxide it Eq. (2), while it equals 4 for the ionization of oxygen.

$$E_{Nernst,i} = \left(\frac{RT_{sK}}{nF}\right)\left(\ln K_{p,ioxi} + \ln\left(\frac{p_i p_{O_2}^{0.5}}{p_j}\right)\right) \quad \text{with}$$

$$i = H_2, \ CO \ \text{and} \ j = H_2O, \ CO_2 \tag{39}$$

The values of the equilibrium constants for the hydrogen and carbon monoxide oxidation reaction were taken from [20]. The tabulated values were compiled to yield two fit correlations, which both have the form of Eq. (40):

$$X = y_0 + A_1 \exp\left(\frac{-T_{sK}}{t_1}\right) + A_2 \exp\left(\frac{-T_{sK}}{t_2}\right) + A_3 \exp\left(\frac{-T_{sK}}{t_3}\right) \tag{40}$$

X denotes either the equilibrium constant of the hydrogen oxidation or of the carbon monoxide oxidation, depending on the employed set of fit correlation coefficients, Table 1. Fig. 5 depicts, that the Nernst voltages of the hydrogen and carbon monoxide oxidation minus the current density-dependent voltage losses have to equal the operational voltage of the fuel cell (E_{op}):

$$E_{op} = E_{Nernst,i} - \eta_{act,i} - \eta_{diff,i} - \eta_{act,O_2} - \eta_{diff,O_2} - \eta_{ohm} \quad \text{with}$$

$$i = H_2, \ CO \tag{41}$$

Hence, the model must distinguish currents originating from the oxidation of hydrogen, I_{H_2}, or of carbon monoxide, I_{CO}, which sum up to the total produced current, I_{tot}:

$$I_{tot} = I_{H_2} + I_{CO} \tag{42}$$

From Eq. (41) and Fig. 5 it can be seen, that a current originating from, e.g. carbon monoxide oxidation can only be produced, when the according Nernst voltage minus the voltage losses of the oxygen electrochemistry and the ohmic losses due to an already flowing current originating from hydrogen oxidation stills yields a positive value.

2.4.1. Activation polarization

Even when no net current is drawn from the fuel cell, the electrochemical reactions, Eqs. (43) and (44) (anode) and Eq. (45) (cathode), occur at equal rates in both directions:

$$H_2 + O^{2-} \leftrightarrow H_2O + 2e^- \tag{43}$$

$$CO + O^{2-} \leftrightarrow CO_2 + 2e^- \tag{44}$$

$$O_2 + 4e^- \leftrightarrow 2O^{2-} \tag{45}$$

The so-called exchange current represents the current flowing in both directions at equilibrium conditions. In order to generate a net current into either direction a certain potential needs to be applied. This potential is referred to as activation polarization, η_{act}, and mathematically best described by the Butler–Volmer equation [21]:

$$I = I_0 \left[\exp\left(\beta\frac{nF\eta_{act}}{RT_{sK}}\right) - \exp\left(-(1-\beta)\frac{nF\eta_{act}}{RT_{sK}}\right)\right] \tag{46}$$

The Butler–Volmer equation comprises two important model parameters. The first parameter is the transfer coefficient β, which represents the part of the change in polarization leading to a change in the reaction rate constant. For fuel cell applications and in our
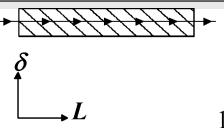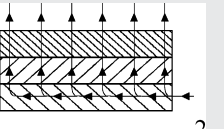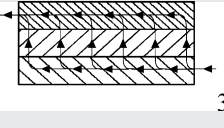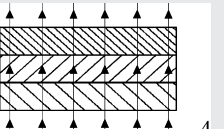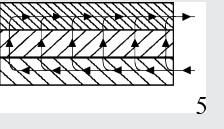
Table 1
Coefficients of the equilibrium constant fit correlation for hydrogen and carbon monoxide oxidation

Coefficient	Hydrogen oxidation	Carbon monoxide oxidation
y_0	−1.093	−3.020
A_1	42.296	376.372
t_1	1297.858	94.704
A_2	106.613	143.468
t_2	319.283	284.902
A_3	284.347	51.766
t_3	107.556	1179.242

Table 2
Equivalent resistance formulas for five cell sub-units with the arrowed lines indicating the current flow path from cathode to anode [25]

Cell sub-unit	Geometry factor J	Resistance R ($\Omega\,\mathrm{m}$)
1	–	$\dfrac{\rho L}{\delta}$
2	$L\sqrt{\dfrac{\rho_{\mathrm{ca}}/\delta_{\mathrm{ca}}}{\rho_{\mathrm{el}}\delta_{\mathrm{el}}}}$	$\sqrt{\dfrac{\rho_{\mathrm{el}}\delta_{\mathrm{el}}(\rho_{\mathrm{ca}}/\delta_{\mathrm{ca}})}{\tanh J}}$
3	$L\sqrt{\dfrac{1}{\rho_{\mathrm{el}}\delta_{\mathrm{el}}}\left(\dfrac{\rho_{\mathrm{an}}}{\delta_{\mathrm{an}}}+\dfrac{\rho_{\mathrm{ca}}}{\delta_{\mathrm{ca}}}\right)}$	$\dfrac{((\rho_{\mathrm{an}}/\delta_{\mathrm{an}})^2+(\rho_{\mathrm{ca}}/\delta_{\mathrm{ca}})^2)\cdot\cosh J+(\rho_{\mathrm{an}}\rho_{\mathrm{ca}}/\delta_{\mathrm{an}}\delta_{\mathrm{ca}})\cdot(2+J\cdot\sinh J)}{\sqrt{(1/\rho_{\mathrm{el}}\delta_{\mathrm{el}})\cdot\sqrt[3]{(\rho_{\mathrm{an}}/\delta_{\mathrm{an}})+(\rho_{\mathrm{ca}}/\delta_{\mathrm{ca}})\cdot\sinh J}}}$
4	–	$\dfrac{\rho_{\mathrm{an}}\delta_{\mathrm{an}}+\rho_{\mathrm{el}}\delta_{\mathrm{el}}+\rho_{\mathrm{ca}}\delta_{\mathrm{ca}}}{L}$
5	$L\sqrt{\dfrac{1}{\rho_{\mathrm{el}}\delta_{\mathrm{el}}}\left(\dfrac{\rho_{\mathrm{an}}}{\delta_{\mathrm{an}}}+\dfrac{\rho_{\mathrm{ca}}}{\delta_{\mathrm{ca}}}\right)}$	$\sqrt{\dfrac{\rho_{\mathrm{el}}\delta_{\mathrm{el}}((\rho_{\mathrm{an}}/\delta_{\mathrm{an}})+(\rho_{\mathrm{ca}}/\delta_{\mathrm{ca}}))}{\tanh J}}$

model, the value is assumed to be 0.5 [21,22]. The second parameter is the exchange current density I_0, which represents the forward and reverse electrode reaction rate at the equilibrium potential. High exchange current densities mean a high electrochemical reaction rate and low activation losses [23]. A large number of models to calculate the exchange current density at the anode and cathode can be found in the literature. In the present work, the anode exchange current density is calculated using Eq. (47) for the hydrogen and the carbon monoxide electrochemistry. The exponents of the molar fractions near to the stoichiometry of the anodic electrochemical reactions result in a direct proportional dependence of the anode exchange current density to the educt and an inversely proportional dependence to the product partial pressures. With the inverse dependency of the activation losses to the exchange current density, the exponents of the molar fractions yield lower activation losses with increased educt or decreased product partial pressures and vice versa [22]. The cathode exchange current density is given by Eq. (48). The exponent of the molar fraction yields lower cathode activation losses with increased oxygen partial pressures.

$$I_{0,\mathrm{an},i}=\gamma_{\mathrm{an},i}\left(\frac{p_{\mathrm{i}}}{p}\right)\left(\frac{p_{\mathrm{j}}}{p}\right)^{-0.5}\exp\left(\frac{-E_{\mathrm{act},\mathrm{an},i}}{RT_{\mathrm{sK}}}\right)\quad\text{with}$$

$$\mathrm{i}=\mathrm{H_2},\ \mathrm{CO}\ \text{and}\ \mathrm{j}=\mathrm{H_2O},\ \mathrm{CO_2} \tag{47}$$

$$I_{0,\mathrm{ca}}=\gamma_{\mathrm{ca}}\left(\frac{p_{\mathrm{O_2}}}{p}\right)^{0.25}\exp\left(\frac{-E_{\mathrm{act},\,\mathrm{ca}}}{RT_{\mathrm{sK}}}\right) \tag{48}$$

It has to be emphasized, that due to the implicit character of the Butler–Volmer equation its solution can only be determined numerically. This effort is however justified by higher accuracy compared to simplified equations such as the Tafel equation [24].

2.4.2. Ohmic polarization

Electronic currents through the electrodes and interconnects as well as ionic currents through the electrolyte induce frictional heat and thereby voltage losses. The calculation of the ohmic voltage losses simply follows Ohm's law:

$$\eta_{\mathrm{ohm}}=R_{\mathrm{equiv}}I_{\mathrm{tot}} \tag{49}$$

The equivalent resistance (R_{equiv}) of SOFCs depends on the geometry and the conductivity of the current conducting components; see Eqs. (4)–(7). In the present model, the area specific equivalent resistance (ASR) is approximated using the transmission line model instead of calculating it via the numerical solution of the Laplace equation. The methodology was developed by Nisancioglu [25] and others [26], and features a high flexibility towards different fuel cell designs. The general idea of the transmission line model is that complex geometries can be described by a set of five standard cell sub-units. Each of these cell sub-units has a characteristic current
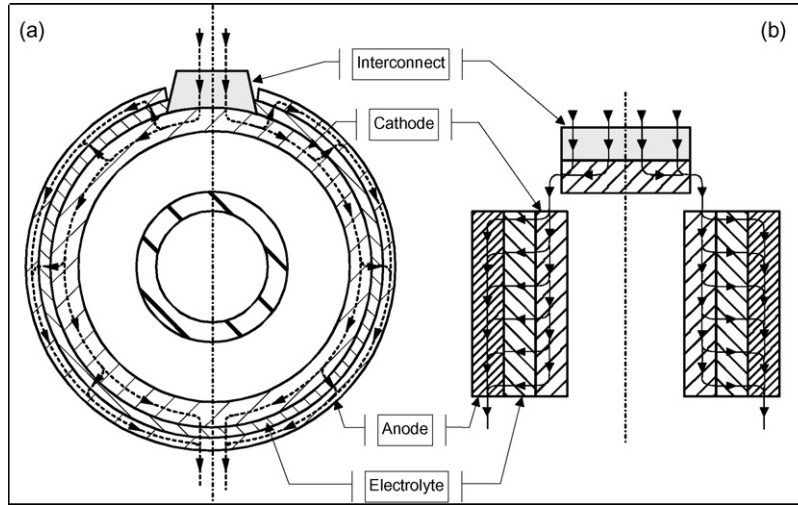
Fig. 6. Cross section of the standard tubular design (a) and transmission line model (b).

path pattern and according analytical formula for the equivalent resistance calculation, Table 2.

2.4.2.1. Application to tubular geometry. Fig. 6 shows the cross section with current paths of the tubular geometry considered in our model, Fig. 6a. The transmission line model approximation, Fig. 6b, consists of two type 3 cell sub-units connected in parallel, representing the two halves of the AEC tube, and one type 2 cell sub-unit, representing the interconnect area, connected in series. Due to the perfect symmetry of the tubular geometry, the equivalent resistance is only calculated for one half-cell and then divided by two. The length of the type 3 cell sub-unit (L_e) for one half-cell is calculated according to Eq. (50) and for the cell sub-unit type 2 (L_{ic}) according to Eq. (51):

$$L_e = \pi r_{m,AEC}(1 - x_{t,ic}) \tag{50}$$

$$L_{ic} = \pi r_{m,AEC} x_{t,ic} \tag{51}$$

The resistance of one half of the cell tube (R_e) is then given by

$$R_e = \frac{((\rho_{an}/\delta_{an})^2 + (\rho_{ca}/\delta_{ca})^2)\cosh J_e + (\rho_{an}\rho_{ca}/\delta_{an}\delta_{ca})(2 + J_e \sinh J_e)}{\sqrt{(1/\rho_{el}\delta_{el})}\sqrt[3]{(\rho_{an}/\delta_{an}) + (\rho_{ca}/\delta_{ca})}\sinh J_e} \quad \text{with}$$

$$J_e = L_e \sqrt{\frac{1}{\rho_{el}\delta_{el}} \left(\frac{\rho_{an}}{\delta_{an}} + \frac{\rho_{ca}}{\delta_{ca}}\right)} \tag{52}$$

The resistance of the interconnect (R_{ic}) is calculated according to

$$R_{ic} = \frac{\sqrt{\rho_{ic}\delta_{ic}(\rho_{ca}/\delta_{ca})}}{\tanh J_{ic}} \quad \text{with } J_{ic} = L_{ic}\sqrt{(1/\rho_{el}\delta_{el})(\rho_{ca}/\delta_{ca})} \tag{53}$$

The equivalent resistance is then calculated following Kirchhoff's law for in-series connection. In order to obtain the ASR value for the calculation of the ohmic voltage loss using a current density, the equivalent resistance is multiplied with the electrochemically active circumferential length of the cell tube:

$$R_{t,equiv} = l_{t,elact}(R_e + R_{ic}) \tag{54}$$

2.4.2.2. Application to triangular geometry. The triangular geometry exhibits current paths which can be described using the same approach as for the standard tubular cell, Fig. 7. The cell sub-unit lengths, L_e and L_{ic}, are given by

$$L_{D8,e} = 0.5 l_{D8,elact} \tag{55}$$

$$L_{D8,ic} = \frac{w_{D8}}{2n_{tri}} \tag{56}$$

The ASR is obtained by multiplying the equivalent resistance with half of the electrochemically active length of the repeat element:

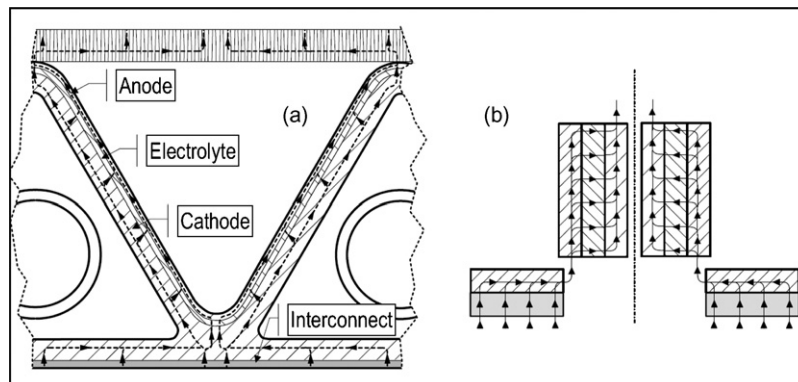$$R_{D8,equiv} = 0.5 l_{D8,elact}(R_e + R_{ic}) \tag{57}$$

Fig. 7. Cross section of the triangular tube cell design (a) and transmission line model (b).
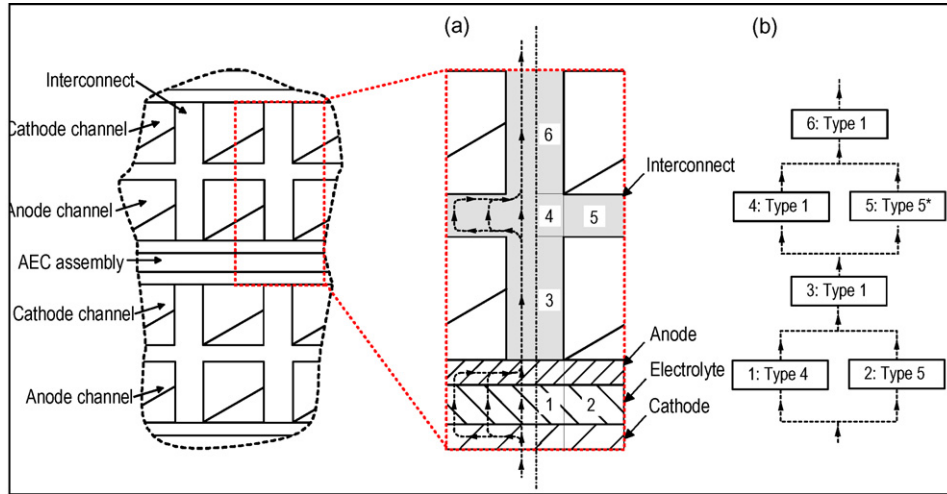
Fig. 8. Cross section of the considered planar cell design (a) and transmission line model (b).

2.4.2.3. Application to planar geometry. Fig. 8 shows a cut out of the considered planar stack and the cross-section of a repeating structure with current paths, Fig. 8a, and transmission line model approximation, Fig. 8b. The equivalent resistance of the repeat element includes six cell sub-units. In our model, the current flow through the AEC assembly is divided into a sub-unit type 4 (R_1) and type 5 (R_2):

$$R_1 = \frac{2(\rho_{ca}\delta_{ca} + \rho_{el}\delta_{el} + \rho_{an}\delta_{an})}{w_c/(n_{ch} - w_{ch})} \tag{58}$$

$$R_2 = \frac{\sqrt{\rho_{el}\delta_{el}((\rho_{an}/\delta_{an}) + (\rho_{ca}/\delta_{ca}))}}{\tanh J_2} \quad \text{with}$$

$$J_2 = \frac{w_{ch}}{2}\sqrt{\frac{1}{\rho_{el}\delta_{el}}\left(\frac{\rho_{an}}{\delta_{an}} + \frac{\rho_{ca}}{\delta_{ca}}\right)} \tag{59}$$

The two cell sub-units are connected in parallel. The interconnect contacts anode and cathode of two adjacent AEC assemblies. The resistances of the interconnect ribs on the anode (R_3) and cathode (R_6) side are calculated using type 1 cell sub-units:

$$R_3 = \frac{2\rho_{ic}h_{p,an}}{(w_c/n_{ch}) - w_{ch}} \tag{60}$$

$$R_6 = \frac{2\rho_{ic}h_{p,ca}}{(w_c/n_{ch}) - w_{ch}} \tag{61}$$

The resistance of the bar between adjoining ribs is calculated by assuming a parallel connection of a type 1 cell sub-unit (R_4) and a modified type 5* cell sub-unit (R_5) [27]:

$$R_4 = \frac{2\rho_{ic}((h_{ic,an} + h_{ic,ca}) - (h_{p,an} + h_{p,ca}))}{(w_c/n_{ch}) - w_{ch}} \tag{62}$$

$$R_5 = \frac{\rho_{ic}}{0.41(1 - \exp(-0.6(w_{ch}/((h_{ic,an} + h_{ic,ca}) - (h_{p,an} + h_{p,ca})))))} \tag{63}$$

Finally, the equivalent circuit depicted in Fig. 8 yields Eq. (64). Similar to the other geometries, the ASR is multiplied with the electrochemically active length of the repeat structure.

$$R_{p,eqiv} = \left(\frac{w_{ce}}{n_{ch}}\right)\left(\left(\frac{1}{R_1} + \frac{1}{R_2}\right)^{-1} + R_3 + \left(\frac{1}{R_4} + \frac{1}{R_5}\right)^{-1} + R_6\right) \tag{64}$$

2.4.3. Diffusion polarization

The diffusion polarization results from the difference of the Nernst voltage calculated for the reactant partial pressures in the bulk gas phase and at the reaction sites located at the triple phase boundary (TPB) where electrolyte and electrode material as well as reactant gases meet. The partial pressures of the educts are generally lower while those of the products are generally higher at the TPB than in the bulk gas phase. The exact partial pressure values depend on the local current density and the material parameters of the porous electrodes through which the educts and products have to diffuse in order to get to the TPB. The current density determines the concentration gradient between the TPB and the bulk gas phase. The material parameters of the porous electrodes include tortuosity, porosity and pore radius. These material parameters together with the fuel composition determine the effective diffusion coefficient which is required to calculate the partial pressures at the TPB using e.g. Fick's law of diffusion. Concentration polarization becomes important for highly diluted fuel gases and at high current densities, where they increase against an asymptotic maximum. At this specific point a further increase of the current is impossible since the reactant partial pressures at the TPB equal zero due to instant conversion.

Our model considers diffusion limitation in the anode and the cathode. At the anode, the educts and the products of the electrochemical reactions diffuse with equal rates to the TPB and back into the gas flow channel respectively. This equimolar counterflow diffusion yields a zero net diffusion flux. Applying Fick's law of diffusion by assuming, that the electrochemical reaction rate equals the mass flux via diffusion, the partial pressures of educts and products at the TPB can be straightforwardly calculated based on the partial pressures in the bulk gas phase according to

$$p_i^{TPB} = p_i \mp \left(\frac{RT_{aK}I\delta_{an}\tau_{an}}{nFD_{eff}\varepsilon_{an}}\right) \quad \text{with} \quad - \text{ for } i = H_2, \text{ CO and}$$

$$+ \text{ for } i = H_2O, \text{ CO}_2 \tag{65}$$

The effective diffusion coefficients, D_{eff,H_2} and $D_{eff,CO}$, are calculated based on binary molecular diffusion coefficients of hydrogen and carbon monoxide with all other considered species in the gas mixture and the Knudsen diffusion coefficient. The binary molecular diffusion coefficients are summed up to yield the effective molecular diffusion coefficient according to Eq. (3). For the calculation

of the effective diffusion coefficient it is assumed, that Knudsen and molecular diffusion occur in parallel. Therefore, the Bosanquet formula was implemented in the present model:

$$D_{\text{eff,i}} = \frac{D_{\text{m,i−mix}} \cdot D_{K,i}}{D_{\text{m,i−mix}} + D_{K,i}} \quad \text{with } i = H_2, \ CO \tag{66}$$

Knowing the partial pressures of the educts and products in the bulk gas phase and at the TPB, the diffusion voltage losses can be computed according to

$$\eta_{\text{diff,i}} = \left(\frac{RT_{\text{sK}}}{nF}\right) \ln\left(\frac{p_i p_j^{\text{TPB}}}{p_j p_i^{\text{TPB}}}\right) \quad \text{with } i = H_2, \ CO \text{ and}$$

$$j = H_2O, \ CO_2 \tag{67}$$

At the cathode, only oxygen takes part in the electrochemical reactions, where it is consumed without forming products.

$$A\frac{p_{O_2}^{\text{TPB}} - p}{D_{K,O_2}(\alpha p_{O_2}^{\text{TPB}} - p) - D_{m,O_2-N_2}} = \exp(I_{\text{tot}} T_{\text{cK}} B) \quad \text{with}$$

$$A = \frac{D_{K,O_2}(\alpha p_{O_2} - p) - D_{m,O_2-N_2}}{p_{O_2} - p} \quad \text{and}$$

$$B = \frac{\tau_{\text{ca}} R \delta_{\text{ca}} (D_{m,O_2-N_2} - D_{K,O_2}(\alpha - 1))}{\varepsilon_{\text{ca}} 2nF D_{m,O_2-N_2} D_{K,O_2 \ p}} \quad \text{and} \quad \alpha = 1 - \left(\frac{M_{O_2}}{M_{N_2}}\right) \tag{68}$$

Eq. (68) was implemented in our model for the implicit calculation of the partial pressure of oxygen at the cathode TPB [28]. In contrast to the diffusion at the anode, the effective diffusion coefficient is calculated for the non-dilute two-component gas mixture at the cathode according to [29] which includes the relation between the molecular masses, α, of the components nitrogen and oxygen. The diffusion voltage loss at the cathode electrode is calculated analogously to the anode electrode:

$$\eta_{\text{diff,}O_2} = \left(\frac{RT_{\text{sK}}}{2nF}\right) \ln\left(\frac{p_{O_2}}{p_{O_2}^{\text{TPB}}}\right) \tag{69}$$

2.5. Mass balance model

The current density values computed by the electrochemical performance model are related to the reactions Eqs. (43)–(45) via the Faraday law yielding the area specific reaction rates of the electrochemical reactions. In the present model, the axial length of the gas channels was defined as the integration variable. In order to account for the two-dimensional distribution of the electrochemical reactions, the area specific reaction rate has to be multiplied with the electrochemically active length of the considered fuel cell design, l_{elact}, so as to be converted to the integration length specific reaction rate. Accordingly, Eqs. (70) and (71) were applied in this model:

$$r_{\text{i,oxi}} = l_{\text{elact}} \left(\frac{I_i}{2F}\right) \quad \text{with } i = H_2, \ CO \tag{70}$$

$$r_{O_2 \text{ ion}} = l_{\text{elact}} \left(\frac{I_{\text{tot}}}{4F}\right) \tag{71}$$

Besides the mentioned electrochemical reactions, this model considers water–gas-shift, Eqs. (72) and (73), and methane steam reforming reactions:

$$CO + H_2O \leftrightarrow CO_2 + H_2 \tag{72}$$

$$CO_2 + H_2 \leftrightarrow CO + H_2O \tag{73}$$

$$CH_4 + H_2O \leftrightarrow CO + 3H_2 \tag{74}$$

Table 3
Coefficients of the equilibrium constant fit correlation for water–gas-shift and methane steam reforming reactions

Coefficient	Water–gas-shift reaction
y_0	−2.08873
A_1	9.5544
t_1	354.50643
A_2	6.81354
t_2	758.72139
A_3	45.01004
t_3	134.0971

The reaction rates of the WGS and REV–WGS are computed via Eqs. (75) and (76):

$$r_{\text{WGS}} = 10000.0 \, \text{mol m}^{-1} \text{s}^{-1} \text{bara}^{-2} \ p_{\text{CO}} p_{H_2O} \tag{75}$$

$$r_{\text{REV−WGS}} = 10000.0 \, \text{mol m}^{-1} \text{s}^{-1} \text{bara}^{-2} \ p_{\text{CO}_2} p_{H_2}$$

$$\times \left(1 - \frac{p_{\text{CO}} p_{H_2O}}{K p_{\text{WGS}} p_{\text{CO}_2} p_{H_2}}\right) \tag{76}$$

Table 3 lists the coefficients for the equilibrium constant fit correlation, Eq. (40), of the WGS. The equilibrium constant values were taken from [20]. In contrast to the WGS, the STR was considered as heterogeneous reaction. An applied kinetic model, Eq. (77), was implemented into the model. The implemented applied kinetic model for the methane steam reforming was developed by Drescher [30], who related the reaction rate to the mass of catalyst. Consequently the pre-exponential factor had to be recalculated to an area specific value in order to allow for the application in the present model. We therefore assumed that only the upper 25 microns of the nickel–cermet participate in the steam reforming reactions. All other data for the recalculation were taken from [30] in order to keep the applied kinetic model concise:

$$r_{\text{CH}_4 \text{ STR,Dre}} = \frac{\begin{array}{c}288.52 \, \text{mol m}^{-2} \text{s}^{-1} \text{bara}^{-2} \ p_{\text{CH}_4} \ p_{H_2O} \\ \times \exp(-11000 \, \text{J mol}^{-1}/RT_{\text{sK}})\end{array}}{\begin{array}{c}1 + 16.0 \, 1 \, \text{bara}^{-1} \ p_{\text{CH}_4} + 0.143 \, 1 \, \text{bara}^{-1} \ p_{H_2O} \\ \times \exp(39000 \, \text{J mol}^{-1}/RT_{\text{sK}})\end{array}} \tag{77}$$

Depending on the geometry of the anode gas channel, the diffusion of the reacting species from the bulk gas phase to the catalyst surface can be slower than the actual chemical reaction. Therefore, the partial pressures of the reactants at the catalyst surface can differ significantly from the bulk gas phase. The calculation of the exact reactant partial pressures at the catalyst surface requires the solution of the complete concentration field perpendicular to the gas flow. In order to avoid solving the corresponding partial differential equations, a mass transfer analogy proposed in [11] was used to compute the reactant partial pressure at the catalyst surface:

$$r_{x,\text{diff}} = \frac{\beta_{x,\text{diff}}}{RT_{\text{aK}}}(p_x - p_x^{\text{cs}}) \tag{78}$$

The mass transfer coefficient $\beta_{x,\text{diff}}$ is calculated by considering the analogy of heat and mass transfer according to

$$\beta_{x,\text{diff}} = \frac{D_{\text{m,mix},x}}{d_{\text{t/p,hyd,an}}} Nu \left(\frac{p}{p - p_x}\right) \tag{79}$$

The calculation of the reactant partial pressure at the catalyst surface can be avoided, by considering the diffusion process and the chemical reaction as two processes connected in parallel. Mathematically this requires the introduction of a conversion coefficient for the considered chemical reaction, $\beta_{x,\text{reac}}$, which is based on the reaction rate, r_{reac}, calculated with the bulk gas phase partial

pressures, Eq. (80). Note that the reaction rate is divided by the partial pressure of the diffusion-limited specie, p_x, to the power of its reaction order, ro_x:

$$\beta_{x,\text{reac}} = r_{\text{reac}} \frac{RT_{\text{sK}}}{p_x^{\text{ro}_x}} \tag{80}$$

The diffusion limited and integration length specific reaction rate, $r_{\text{dl-reac}}$, is obtained from

$$r_{\text{dl-reac}} = l_{\text{chact}} \beta_{x,\text{diff-reac}} \frac{p_x^{\text{ro}_x}}{RT_{\text{sK}}} \quad \text{with} \quad \beta_{x,\text{diff-reac}} = \frac{\beta_{x,\text{diff}} \beta_{x,\text{reac}}}{\beta_{x,\text{diff}} + \beta_{x,\text{reac}}} \tag{81}$$

The partial pressure of the diffusion-limited species, p_x, to the power of its reaction order, ro_x, is thus reintroduced. Knowing the reaction rate of all reactions and neglecting axial diffusion mass transport, the spatial distribution of the species along the anode channel can be computed according to the differential equation:

$$\frac{d\dot{n}_i}{dx} = \sum_1^j \nu_{ij} r_j \quad \text{with} \quad i = \text{H}_2, \ \text{CO}, \ \text{etc.}, \ \text{and}$$

$$j = \text{WGS}, \ \text{STR}, \ \text{etc.} \tag{82}$$

The spatial distribution of oxygen and nitrogen in the cathode channel is computed analogously. However, the mass balance equation for oxygen is different for the two modeled flow patterns for the planar cell design, namely co- and counter-flow. In the co-flow case the oxygen content decreases with the axial coordinate when a current is produced. For the counter-flow case, the opposite applies. The different boundary conditions for the considered flow patterns will be addressed in subsequent chapters.

$$\frac{d\dot{n}_{\text{N}_2,\text{ca}}}{dx} = 0.0 \tag{83}$$

$$\frac{d\dot{n}_{\text{O}_2}}{dx} = R_{\text{O}_2} \quad \text{with} \quad R_{\text{O}_2} = -r_{\text{O}_2 \text{ ion}} \ \text{(co-flow) or}$$

$$R_{\text{O}_2} = r_{\text{O}_2 \text{ ion}} \ \text{(counter-flow)} \tag{84}$$

Based on the calculated reaction rates, the mass balance model also computes the related heat source term according to

$$\Delta H_{\text{r}} = r_{\text{H}_2 \text{ oxi}} \Delta H_{\text{R,H}_2 \text{ oxi}} + r_{\text{CO oxi}} \Delta H_{\text{R, CO oxi}} + r_{\text{dl-CH}_4 \text{ STR}} \Delta H_{\text{R, CH}_4 \text{ STR}}$$

$$+ r_{\text{WGS}} \Delta H_{\text{R,WGS}} + r_{\text{REV-WGS}} \Delta H_{\text{R,REV-WGS}} \tag{85}$$

By definition, the heats of reaction are attributed to the solid structure of the fuel cell. The differing heat capacities of educt and product species as well as the different temperature of the gas phase and the solid structure result in an enthalpy flux coupled to the mass flow from the solid structure to the gas phase and vice versa. Eqs. (86)–(88) give the mass transfer coupled enthalpy flux of the educts and products at the anode and the enthalpy flux at the cathode:

$$\dot{Q}_{\text{SH,ed,an}} = \sum_j r_j T_{\text{aK}} \sum_i \nu_{i,\text{ed}} c_{\text{p},i,T_{\text{aK}}} \tag{86}$$

$$\dot{Q}_{\text{SH,prod,an}} = \sum_j r_j T_{\text{sK}} \sum_i \nu_{i,\text{prod}} c_{\text{p},i,T_{\text{sK}}} \tag{87}$$

$$\dot{Q}_{\text{SH,ed,ca}} = r_{\text{O}_2 \text{ ion}} T_{\text{cK}} c_{\text{p,O}_2,T_{\text{cK}}} \tag{88}$$

In these equations, r_j stands for the reaction rate of the different considered heterogeneous reactions, including the electrochemical reactions, occurring at the anode and $r_{\text{O}_2 \text{ ion}}$ represents the reaction rate of reaction Eq. (45).

2.6. Energy balance model

Considering the strong heat exchange mechanisms between the solid cell components, i.e. heat conduction and radiation, and taking into account the compactness of the considered fuel cell designs, the assumption of only one effective solid structure temperature for all solid cell components is reasonable [11]. However, this assumption does not necessarily include the gas phase temperatures due to the weak heat exchange via convection and the negligible radiative heat exchange between solid structure and gas phase. In order to account for these conclusions, the energy balance model determines the axial temperature profile of the solid structure, of the anode gas and cathode gas as well as the air in the air delivery tube in case of a tubular design.
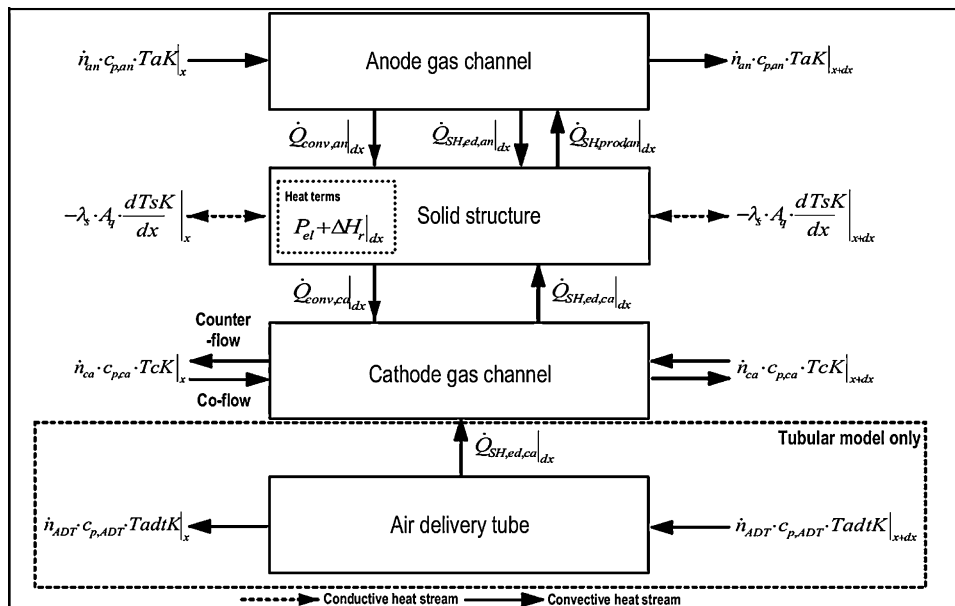

Fig. 9. Outline of the energy balance model.

Fig. 9 depicts the outline of the energy balance model for an infinitesimal control volume with the three balance cases of the planar design, namely the anode and cathode gas channel as well as the solid structure, and the additional fourth balance case of tubular cell designs, namely the air delivery tube.

The energy balance of the anode gas channel includes the sensible heat flow, $\dot{n}_{an*}c_{p,an*}T_{aK}$, entering the control volume at the coordinate x and leaving it at $x + dx$. Further, the enthalpy flux due to the different heat capacity of the educt and product species reacting at the anode are accounted for. The conductive heat stream between solid structure and anode gas channel is computed via Eq. (89):

$$\dot{Q}_{conv,an} = \alpha_{an} l_{circ,an}(T_{aK} - T_{sK}) \quad \text{with} \quad \alpha_{an} = \frac{Nu\,\lambda_{an}}{d_{hyd,an}} \qquad (89)$$

The differential equation describing the axial temperature distribution along the anode gas channel can thus be formulated as follows:

$$\frac{d(\dot{n}_{an}c_{p,an}T_{aK})}{dx} = \dot{Q}_{SH,prod,an} - \dot{Q}_{SH,ed,an} - \dot{Q}_{conv,an} \qquad (90)$$

It should be noted, that this model considers the change of the total molar flow, n_{an}, and the change of the heat capacity, $c_{p,an}$, due to the change of the gas composition over the control volume. In some models found in the literature, only the temperature change is considered by assuming the heat capacity and sometimes also the molar flow are fixed at the inlet conditions of the according control volume [22,31,32]. For coarse discretization aiming at short calculation times, this can affect accuracy.

The energy balance of the solid structure involves the overall heat of reaction, Eq. (85), and the mass transfer coupled enthalpy fluxes at the anode and cathode electrode, Eqs. (86)–(88). Besides, the convective heat flows between the solid structure and anode as well as cathode channel have to be considered. The produced electrical power is considered as source term for the solid structure and is computed according to

$$P_{el} = -l_{elact}I_{tot}E_{op} \qquad (91)$$

The convective heat flow between the cathode gas channel and the solid structure is determined according to Eq. (92). The sign of the convective heat flow is considered positive, when heat is transferred from the solid structure to the cathode gas. This reflects the cooling task of the air flow in the cathode channel:

$$\dot{Q}_{conv,ca} = \alpha_{ca} l_{circ,ca}(T_{sK} - T_{cK}) \quad \text{with} \quad \alpha_{ca} = \frac{Nu\,\lambda_{ca}}{d_{hyd,ca}} \qquad (92)$$

Finally, the energy balance of the solid structure includes solid heat conduction yielding a second order derivate differential equation:

$$\lambda_s A_{cross}\frac{d^2 T_{sK}}{dx^2} = \dot{Q}_{conv,ca} - \dot{Q}_{conv,an} - \dot{Q}_{SH,ed,an} - \dot{Q}_{SH,ed,ca}$$
$$+ \dot{Q}_{SH,prod,an} + \Delta H_r + P_{el} \qquad (93)$$

The differential equation to compute the cathode gas temperature of the planar cell designs is given by

$$\frac{d(\dot{n}_{ca}c_{p,ca}T_{cK})}{dx} = \dot{Q}_{conv,ca} - \dot{Q}_{SH,ed,an} + \dot{Q}_{conv,ADT} \ \text{(co-flow)}$$
$$= \dot{Q}_{SH,ed,an} - \dot{Q}_{conv,ca} \ \text{(counter-flow)} \qquad (94)$$

In principle, the tubular cell designs have a co-flow pattern. However, the design typical air delivery tube, adds one more term to the cathode gas energy balance: the convective heat flow from the air delivery tube to the cathode gas, $\dot{Q}_{conv,ADT}$.

$\dot{Q}_{conv,ADT}$ aggregates the convective heat transport from the cathode air to the air delivery tube (ADT) and from the ADT to the cold air flowing inside the ADT, Eq. (95). In this model, the

Table 4
Mass balance boundary conditions

Mass balance	Planar co-flow	Planar counter-flow	Tubular
Anode gas	$\dot{n}_{an(0)} = \dot{n}_{an,0}$	$\dot{n}_{an(0)} = \dot{n}_{an,0}$	$\dot{n}_{an(0)} = \dot{n}_{an,0}$
Cathode gas	$\dot{n}_{ca(0)} = \dot{n}_{ca,0}$	$\dot{n}_{ca(0)} = \dot{n}_{ca,0}$	$\dot{n}_{ca(0)} = \dot{n}_{ca,0}$
Air delivery tube	–	–	$\dot{n}_{ADT(n)} = \dot{n}_{ca,0}$

two processes are accounted for via an effective heat exchange coefficient, $\alpha_{ADT,eff}$, which was proposed in [33]. The calculation of $\alpha_{ADT,eff}$ includes the solid heat conduction coefficient of the ADT material which leads to either enhanced or reduced convective heat exchange in cold or hot regions of the ADT, respectively.

$$\dot{Q}_{conv,ADT} = \alpha_{ADT,eff} l_{circ,ADT}(T_{adtK} - T_{cK}) \quad \text{with} \quad \alpha_{ADT,eff}$$
$$= \frac{1}{r_{i,ADT}}\left(\frac{1}{r_{i,ADT}\alpha_{ADT}} + \frac{1}{4\lambda_{s,ADT}}\ln\left(\frac{r_{o,ADT}}{r_{i,ADT}}\right) + \frac{1}{r_{o,ADT}\alpha_{ca}}\right)$$
$$\text{and} \quad \alpha_{ADT} = \frac{Nu\,\lambda_{ADT}}{d_{hyd,ADT}} \qquad (95)$$

The energy balance of the air flow inside the ADT can then be formulated as Eq. (96). Since the air flow inside the ADT is not taking part in any chemical or electrochemical reactions, the molar flow is constant. Accordingly the differential equation for the ADT energy balance was simplified in the present model:

$$\dot{n}_{ADT}\frac{d(c_{p,ADT}T_{adtK})}{dx} = \dot{Q}_{conv,ADT} \qquad (96)$$

2.7. Boundary conditions

The mass balance boundary condition values are calculated based on the user-defined operating conditions. The fuel inlet composition is specified in molar fractions of the considered species. The total molar flow of the fuel gas at the cell inlet is either calculated based on a targeted overall current density, $I_{tot,av}$, and related fuel utilization, UF, Eq. (97), or by specifying a lower heating value (LHV)-based input power, P_{in}:

$$\dot{n}_{an,0} = \frac{I_{tot,av}A_{act}}{2F\,UF\,Eq_{H_2}} \quad \text{with} \quad Eq_{H_2} = y_{H_2} + y_{CO} + 4y_{CH_4} \qquad (97)$$

$$\dot{n}_{an,0} = \frac{P_{in}}{LHV_{in}n_{RE}} \qquad (98)$$

The inlet molar flow of the cathode gas is either assigned directly or by specifying an air-to-fuel ratio, λ:

$$\dot{n}_{ca,0} = \frac{\dot{n}_{O_2,stoic}\lambda}{y_{O_2}} \quad \text{with} \quad \dot{n}_{O_2,stoic}$$
$$= \dot{n}_{an,0}(0.5y_{H_2} + 0.5y_{CO} + 2y_{CH_4}) \qquad (99)$$

Depending on the investigated fuel cell design and the considered flow pattern, the mass balance boundary values were assigned to different control volumes (CV), see Table 4 where (0) denotes the first and (n) the last CV. The total molar flow values n_{an}, n_{ca} and n_{ADT} are related to the molar flows of the single species via the user-defined molar fractions.

Besides the inlet molar flow, the present model requires the definition of the gas temperatures at the inlet in order to solve the

Table 5
Gas phase energy balance boundary conditions

Energy balance	Planar co-flow	Planar counter-flow	Tubular
Anode gas	$T_{aK(0)} = T_{an,in}$	$T_{aK(0)} = T_{an,in}$	$T_{aK(0)} = T_{an,in}$
Cathode gas	$T_{cK(0)} = T_{ca,in}$	$T_{cK(n)} = T_{ca,in}$	$T_{cK(0)} = T_{adtK(0)}$
Air delivery tube	–	–	$T_{adtK(n)} = T_{ADT,in}$

Table 6
Fuel and cathode gas compositions of the BMT

Specie	Unit	Fuel gas IEA 1	Fuel gas IEA 2	Cathode gas	Source
Hydrogen		90.00	26.26	–	
Carbon monoxide		–	2.94	–	
Carbon dioxide		–	4.36	–	
Water	vol.%	10.00	49.34	–	[34]
Methane		–	17.10	–	
Nitrogen		–	–	79.00	
Oxygen		–	–	21.00	

Table 7
Geometrical input data of BMT

Model input data	Unit	Value	Source
Macrogeometry of planar cell			
Flow design	–	Co- and counter-flow	
Number of cells in stack	–	1	
Number of gas channels per cell	–	18	
Cell width	m	0.1	
Cell length	m	0.1	
Gas channel width	m	0.003	[34]
Anode and cathode channel height	m	0.001	
Height of IC on anode/cathode side	m	0.00125	
Area covered by IC participating in electrochemistry	%	100.0	
Chemically act. area covered by IC	%	0.0	
Microgeometry of planar cell			
Support design	–	Electrolyte	
Anode thickness	μm	50.0	
Electrolyte thickness	μm	150.0	[34]
Cathode thickness	μm	50.0	

energy balance equation of the gas channels. The inlet gas temperatures of the anode, the cathode and eventually of the air deliver tube are user-defined values and assigned as shown in Table 5. In case of the tubular cell design, the boundary conditions of the cathode gas channel ensure the continuity between the temperature and the molar flow of the air flow exiting the air delivery tube and entering the cathode gas channel.

Owing to the considered solid heat conduction, the energy balance of the solid structure includes a second derivate term. Hence, the solution of each CV depends on the solutions of the neighboring CVs. Consequently, boundary conditions have to be defined at both ends of the integration region. The differential equation applying at the left boundary (first CV of the integration region) is given by

$$\lambda_s A_{cross} \frac{dT_{sK}}{dx} = \dot{Q}_{hloss} \qquad (100)$$

$\dot{Q}_{hloss}$ represents the heat loss flow to the surroundings. At the right boundary, the source terms of the last CV of the integration region have to be taken into account:

$$\lambda_s A_{cross} \frac{dT_{sK}}{dx} = (\dot{Q}_{conv,ca} - \dot{Q}_{conv,an} - \dot{Q}_{SH,ed,an} - \dot{Q}_{SH,ed,ca}$$
$$+ \dot{Q}_{SH,prod,an} + \Delta H_r + P_{el}) dx - \dot{Q}_{hloss} \qquad (101)$$

For the tubular design the cell ends are generally assumed adiabatic. In contrast, our model features the possibility to assume adiabatic cell ends or conductive heat losses at the cell ends of planar cells. Where adiabatic cell ends are assumed for the simulation of a perfect insulation, $\dot{Q}_{hloss}$ is set to zero. Assuming conductive heat losses through insulation, Eq. (102) applies:

$$\dot{Q}_{hloss} = \alpha_{insul} A_{t/p,cross}(T_{sK} - T_{amb}) \qquad (102)$$

3. Model validation

3.1. Planar geometry

A verification of our model is carried out by comparing the computed results to a benchmark test (BMT). The BMT was defined in an International Energy Agency (IEA) program for the numerical simulation of SOFCs with planar geometry [34]. In total, nine different academic and industrial institutions participated in the BMT. The independently developed models showed good agreement concerning the predicted physical behavior for two fuel gas compositions, in detail humidified hydrogen and 30% pre-reformed methane, Tables 6 and 7 gives the BMT macro and micro geometry data of the considered planar, electrolyte supported SOFC. Table 8 shows the operational conditions of the considered SOFC defined by the BMT participants.

The BMT participants agreed to consider only ohmic losses for a better comparability of the model results. The specific ohmic resistances of the ceramic components were calculated according to Eqs. (4)–(7). For the planar SOFC, ceramic bipolar plates were assumed. Further, the applied kinetics data for the steam reforming reaction

Table 8
Operational conditions of BMT

Model input data	Unit	Value	Source
Operational conditions			
Targeted mean current density	A m^{-2}	3000.0	
Targeted fuel utilization	%	85.0	
Air-to-fuel ratio	–	7.0	
Fuel gas inlet temperature	K	1173.15	[34]
Cathode gas inlet temperature	K	1173.15	
Ambient temperature	K	293.15	
System pressure	bara	1.01325	

Table 9
Energy balance input data of BMT

Model input data	Unit	Value	Source
Solid heat conduction			
Heat conductivity of anode		2.0	
Heat conductivity of electrolyte	$W\,m^{-1}\,K^{-1}$	2.0	[34]
Heat conductivity of cathode		2.0	
Heat conductivity of interconnect		2.0	
Convective heat transfer			
Nusselt number	–	4.0	[34]

(STR) were prescribed:

$$r_{CH_4\,STR,Ach} = 4274.0\,\mathrm{mol\,m^{-2}\,s^{-1}\,bara^{-1}}\,p_{CH_4}$$

$$\times \exp\left(\frac{-82000\,\mathrm{J\,mol^{-1}}}{RT_{sK}}\right) \tag{103}$$

Table 9 gives the BMT parameter used for the energy balance calculations. Besides, several assumptions were defined for the BMT, Table 10. The most important assumptions were that the activation polarization losses are equal to the ohmic loss of the electrolyte and that diffusion losses are negligible. For this reason, a validation of activation and diffusion loss model parameters is not possible using the BMT. Furthermore, the change of the molar flow and the heat capacity of the gas mixture was neglected in the calculation of the gas phase energy balance. Instead the calculations were performed with a simplified definition of the

Table 10
Model settings of BMT

Model settings	Description
Electrochemical loss model settings	
Considered electrochemical active species	Hydrogen
Activation polarization equation	Equal to ohmic loss of electrolyte
Energy balance settings	
Solid heat transfer mechanism	Non-isothermal with solid heat conduction
Coupled heat and mass transport	Considered
Heat loss mechanism at outer surface	Conduction through insulating plates
Heat capacity and heat of reaction correlation	Published in [11]
Definition of sensible heat gradient	$\dot{n}\cdot c_p\vert_x \cdot \frac{dT}{dx}$

sensible heat gradient by holding the molar flow and heat capacity constant at the value of the antecedent control volume for the respective control volume. Further information can be found in [34].

Fig. 10 shows the comparison of the results of our model for the co-flow pattern considering both IEA fuel gases, Table 6. The terms "Minimum value" and "Maximum value" refer to the minimum and maximum values among all the BMT participants, whereas "Own" refers to the results obtained from our model. Fig. 11 shows the comparison of the results for the counter-flow pattern. It can be seen, that our model behaves physically correct and that there is no systematic discrepancy to the results of other participants in
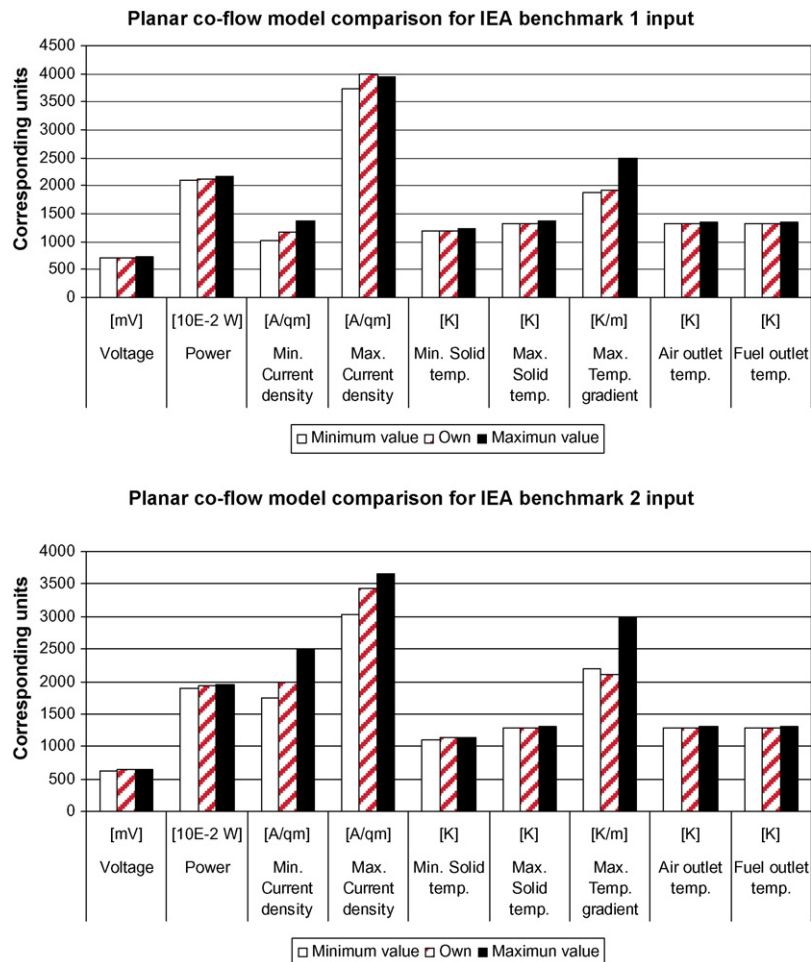
Planar co-flow model comparison for IEA benchmark 1 input

Planar co-flow model comparison for IEA benchmark 2 input

Fig. 10. Comparison of co-flow model results with BMT results for fuel compositions IEA 1 and IEA 2.
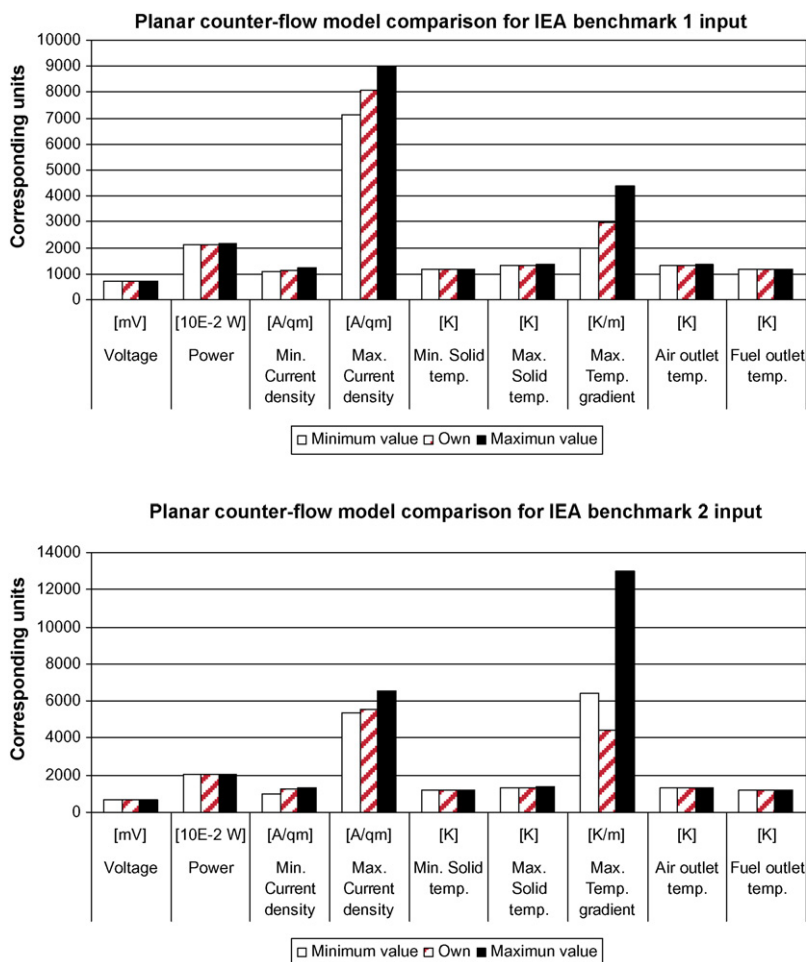
Fig. 11. Comparison of counter-flow model results with BMT results for fuel compositions IEA 1 and IEA 2.

the BMT. It is concluded, that our model is a reliable tool for the simulation of planar SOFCs.

3.2. Tubular geometry

The aim of validating our model for the standard tubular cell geometry is to assure that the generalized approach, which is based on characteristic lengths and areas, has been properly adapted to the tubular cell design. Although the most important parts of the model code were already verified using the BMT for the planar geometry, there is still a need to also check the equations involved in the calculation of the activation and diffusion losses as those were excluded from the BMT. The geometric data for the description of the standard tubular cell is given in Table 11.

The experimental voltage–current curves used for the validation were published in [35]. The characterized standard tubular cell was operated with a fuel gas mixture consisting of 89 vol.% H_2 and 11 vol.% H_2O at three different cell temperatures, 900 °C, 940 °C and 1000 °C with a fuel utilization of 85% and an air-to-fuel ratio of 4. The latter feature allows checking for the correct prediction of temperature effects and hence makes this data set predestined for model validation purpose. Model results obtained for other temperatures can be assumed valid, in case the model reliably predicts the temperature induced effects of the validation case. When model validation is carried out with data sets measured at a single temperature, the results are only valid for this temperature and extrapolated results have to be considered less reliable.

For the simulation, the gas inlet temperatures were assumed 100 K lower than the respective mean cell temperature [28]. The heat transfer calculation input data is given in Table 12. The electrochemical loss model parameters are given in Table 13.

The conductivity of the anode, electrolyte and cathode are calculated using the same correlations as in the BMT. The diffusion polarization loss parameters were taken from Stiller [31]. However, the cathode electrode tortuosity was slightly increased from

Table 11
Geometrical input data for standard tubular cell model

Model input data	Unit	Value	Source
Macrogeometry of tubular cell			
Flow design	–	Co-flow with air delivery tube	
Cell tube length	m	1.5	[28,31]
Inner radius of air delivery tube	m	0.0025	
Outer radius of air delivery tube	m	0.004	
Inner radius of cell tube	m	0.00866	
Thickness of virtual fuel channel (depends on stacking of cell tubes)	m	0.0023	
Percentage of circumferential length of cell tube covered by IC	%	10.0	
Microgeometry of planar cell			
Support design	–	Cathode	
Anode thickness	μm	100.0	
Electrolyte thickness	μm	40.0	[28,31]
Cathode thickness	μm	2200.0	

Table 12
Energy balance input data for standard tubular cell model validation

Model input data	Unit	Value	Source
Solid heat conduction			
Heat conductivity of anode		6.23	
Heat conductivity of electrolyte		2.7	
Heat conductivity of cathode	$W\,m^{-1}\,K^{-1}$	9.6	[31]
Heat conductivity of air delivery tube		11.8	
Nusselt number	–	4.0	

Table 13
Electrochemical loss model input data for tubular and Delta8 cell model

Model input data	Unit	Value	Source
Activation polarization			
H_2 oxidation activation energy	$J\,mol^{-1}$	110000.0	
H_2 oxidation pre-exponential factor	$A\,m^{-2}$	7000000000.0	[13]
CO oxidation activation energy	$J\,mol^{-1}$	110000.0	
CO oxidation pre-exponential factor	$A\,m^{-2}$	5000000000.0	[11,13]
O_2 reduction activation energy	$J\,mol^{-1}$	149500.0	
O_2 reduction pre-exponential factor	$A\,m^{-2}$	10260000000.0	[28]
Ohmic polarization			
Electric conductivity of anode	$1\,\Omega^{-1}\,m^{-1}$	T-dependent, Eq. (4)	[12]
Ionic conductivity of electrolyte	$1\,\Omega^{-1}\,m^{-1}$	T-dependent, Eq. (5)	
Electric conductivity of cathode	$1\,\Omega^{-1}\,m^{-1}$	T-dependent, Eq. (6)	
Electric conductivity of interconnect	$\Omega\,m$	2.0E−7	[28]
Diffusion polarization			
Porosity of anode	–	0.4	
Tortuosity of anode	–	3.0	
Pore diameter of anode and cathode	m	1.0E−6	[31]
Porosity of cathode	–	0.5	
Tortuosity of cathode	–	1.8	–

1.5 to 1.8 in order to better reproduce the diffusion limitation at high current densities. The activation polarization parameters for the hydrogen oxidation and for the oxygen ionization were taken from Campanari [13], and Thorud [28], respectively. The activation loss parameters for the carbon monoxide oxidation were calculated based on those of the hydrogen oxidation and the relation proposed in [11].

In the following the model results are compared to the experimental voltage–current curves. As the same voltage–current curves were used for model validation purpose in [28], the detailed discussion of the reasons for the difference between the model results and the measurement, carried out in [28], is not repeated at this point. However, the higher accuracy of the present model is highlighted.
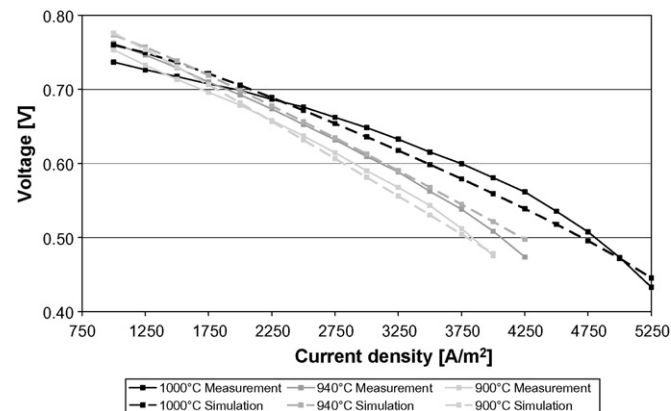

Fig. 12. Comparison of simulated and measured voltage–current curve of a standard tubular cell measured at mean cell temperature of 900 °C, 940 °C and 1000 °C.

Fig. 12 shows the comparison of simulated (dashed line) and measured (full line) voltage–current density (U–I) characteristics of the tubular cell operated at 900 °C, 940 °C and 1000 °C. The mean variance of the predicted voltage for 900 °C operational mean cell temperature compared to the measured values is 1.6% and the maximum variance is below ±3%. For 940 °C the predicted voltage values diverge by less than 1% for small and medium current density values. At higher current density values the variance increases up to 5%. The mean variance between predicted and measured voltage values for 940 °C mean cell temperature is 1.3%. At a mean cell temperature of 1000 °C, the mean variance between predicted and measured voltage values is 2.3% and the maximum variance is below ±4%. In contrast to [28], at high current density values, the present model predicts a slight bend of the U–I curve due to increasing diffusion losses. This phenomenon can be observed more pronounced for the measurement. The prediction of this phenomenon emphasizes that our tubular model behaves physically correct.

It is concluded, that our generalized model was properly adapted to the tubular cell geometry. Further, the activation and diffusion loss model equations and related model parameters proved to yield accurate results.

3.3. Triangular geometry

The published data dealing with Delta8 cells (D8) is scarce as they have only recently been developed. Nevertheless, Table 14 gives the available D8 cell geometrical data. It is important to point out that the geometry of the air delivery tube was not taken from a publication but was assumed to yield an adequate cathode gas channel cross-sectional area. This assumption directly impacts the convective heat transfer between the cathode gas and the air delivery tube. The convective heat transfer between the cathode gas and the solid structure is however dominating in any case, such that the overall impact of this assumption is considered less significant.

The experimental voltage–current curve used for the validation of the triangular cell model was measured using a D8 cell segment [3]. The 1 cm long D8 cell segment was operated under isothermal conditions in an oven at temperatures between 950 °C and 965 °C with fuel and air excess. The fuel mixture consisted of 50 vol.% H_2 and 50 vol.% H_2O, being the expected average gas composition of a full-scale cell operated at 85% fuel utilization with 89 vol.% H_2 and 11 vol.% H_2O. Due to the isothermal conditions and the virtually constant reactant partial pressures along the D8 cell segment, the voltage–current curve was simulated by using the electrochemical performance model without considering the

Table 14
Geometrical input data for Delta8 cell model

| Model input data	Unit	Value	Source
Macrogeometry of tubular cell			
Flow design	–	Co-flow with air delivery tube	–
Cell length	m	1.0	
Cell width	m	0.15	
Triangle half angle	°	30.0	[3]
Number of triangular tubes per cell	–	8	
Inner radius of air delivery tube	m	0.002	–
Outer radius of air delivery tube	m	0.003	–
Microgeometry of planar cell			
Support design	–	Cathode	
Anode thickness	μm	100.0	
Electrolyte thickness	μm	60.0	[37]
Cathode thickness	μm	1500.0	
Interconnect thickness	μm	100.0	
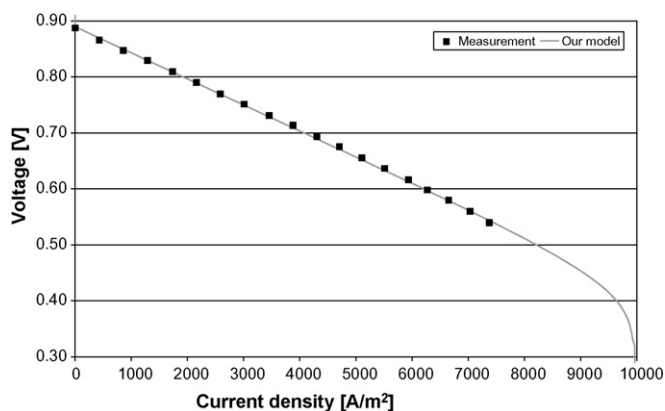
Fig. 13. Comparison of simulated and measured voltage–current curve of a D8 cell segment measured at a temperature between 950 °C and 965 °C.

Fig. 14. Current density distribution of planar, tubular and Delta8 cell.

energy and heat balance. Concerning the model parameters, it was assumed that the anode and cathode materials used for the D8 cells are like those used for the standard tubular cells. Accordingly, the model parameters given in Table 13 apply. Exceptions were the electric conductivity of the interconnect material, which was calculated according to Eq. (7), and the ionic conductivity of the electrolyte, as D8 cells employ scandia-stabilized zirconia (ScSZ) instead of the state-of-the-art yttria-stabilized zirconia (YSZ) as electrolyte material [3]. At temperatures above 900 °C, ScSZ features ionic conductivities about three times higher than YSZ [36]. Hence, the conductivity values computed via Eq. (5) were multiplied by three for the D8 cell segment simulation. Fig. 13 shows the comparison of the measured and the simulated voltage–current curve of the D8 cell segment. The simulation result for 957 °C fits the measured data very well. It is concluded, that the present model was successfully applied to the triangular geometry and that the above discussed assumptions are valid.

4. Performance comparison

Benchmarking of SOFCs is usually performed with humidified hydrogen. The fuel of choice for SOFCs is however pre-reformed natural gas, which, besides electrochemical reactions, involves steam reforming reactions and enhanced heat transfer processes. In order to account for the whole variety of possible interactions between charge, heat and mass transfer processes, the comparison of the

planar, tubular and Delta8 design was conducted considering pre-reformed NG as fuel gas The electrochemical performance model input parameters employed in the planar model are summarized in Table 15. Note that, as only the conversion of hydrogen was considered in [22], no parameters for the carbon monoxide activation polarization were specified. However, in [11] it is stated that the activation potential loss of the electrochemical conversion of carbon monoxide is approximately 1.4 times higher than that for the electrochemical hydrogen conversion. Based on this, the pre-exponential factor for the calculation of the carbon monoxide conversion exchange current density was determined.

For a better comparability of the partial pressure related voltage losses, the fuel utilization and the operational voltage were fixed at 85% and 0.6 V, respectively. Further, the air-to-fuel ratio was fixed at a value of 4.28. The fuel and air inlet temperatures were adjusted to meet the typical mean cell temperature of the investigated cell designs being 950 °C for the planar and Delta8 cell and 1000 °C for the tubular cell.

Fig. 14 shows the current density plotted against the dimensionless cell length of the three investigated cell designs. In average, the electrolyte supported planar cell produces 3468 A m^{-2} while the tubular cell yields 2890 A m^{-2}. The Delta8 cell has the highest current output with 5027 A m^{-2}, which corresponds to 800 W at 0.6 V operational voltage. This value is close to the projected power output of 1000 W at a mean cell temperature of 1000 °C [3], however some improvements will still be necessary to reach this target in case it was defined for natural gas operation of the Delta8 cells.

The shape of the current density distribution is similar for the tubular and the Delta8 cell. The maximum current density is

Table 15
Electrochemical loss model input data for planar cell model

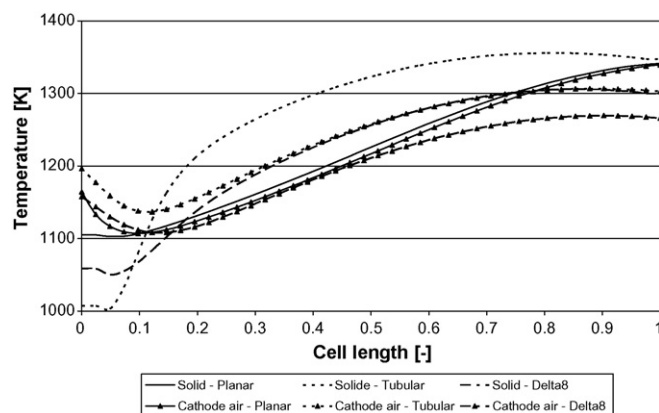| Model input data	Unit	Value	Source
Activation polarization			
H$_2$ oxidation activation energy	J mol^{-1}	120000.0	[22]
H$_2$ oxidation pre-exponential factor	A m^{-2}	2900000000.0	
CO oxidation activation energy	J mol^{-1}	120000.0	[11]
CO oxidation pre-exponential factor	A m^{-2}	2070000000.0	
O$_2$ reduction activation energy	J mol^{-1}	120000.0	[22]
O$_2$ reduction pre-exponential factor	A m^{-2}	7000000000.0	
Ohmic polarization			
Electric conductivity of anode	1 Ω^{-1} m^{-1}	T-dependent, Eq. (4)	
Ionic conductivity of electrolyte	1 Ω^{-1} m^{-1}	T-dependent, Eq. (5)	[12]
Electric conductivity of cathode	1 Ω^{-1} m^{-1}	T-dependent, Eq. (6)	
Electric conductivity of interconnect	1 Ω^{-1} m^{-1}	T-dependent, Eq. (7)	
Diffusion polarization			
Porosity of anode	–	0.5	
Tortuosity of anode	–	3.0	
Pore diameter of anode and cathode	m	1.0E−6	[10]
Porosity of cathode	–	0.5	
Tortuosity of cathode	–	3.0	

Fig. 15. Solid and cathode air temperature distribution of planar, tubular and Delta8 cell.
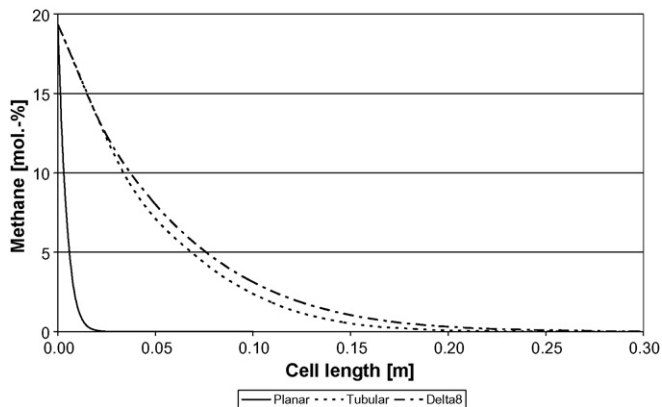
Fig. 16. Methane molar fraction distribution of planar, tubular and Delta8 cell.

Fig. 18. Voltage loss distribution of tubular cell.

reached in the first half of the cell length, while the current density maximum of the planar cell can be observed in the second half. The reason for this can be found in the temperature distribution. Fig. 15 depicts the temperature distribution over the dimensionless cell length. In contrast to the tubular and the Delta8 cell, which feature an air delivery tube cooling the cell outlet region, the solid temperature of the planar cell keeps increasing towards the cell end.

Due to the short cell length of the planar cell, the planar cell design features the highest thermal gradients with maximum values as high as $3.3\,K\,mm^{-1}$. The tubular cell exhibits lower thermal gradients of at most $1.3\,K\,mm^{-1}$. Despite the fact that the Delta8 cell was assumed to have a lower solid heat conductivity coefficient of $2\,W\,m^{-1}\,K^{-1}$ compared to $9.3\,W\,m^{-1}\,K^{-1}$ of the tubular cell, the Delta8 cell shows the lowest thermal gradients with $0.8\,W\,m^{-1}\,K^{-1}$. This can be assigned to the enhanced convective heat exchange between the solid structure and the cathode air due to a smaller hydraulic diameter and the relatively seen bigger heat exchange surface of the cathode gas channel. The same reason applies for the less pronounced reforming cold spot of the Delta8 cell, which is inhibited by the pre-heated cathode air exiting the air delivery tube providing heat for the endothermal reforming reactions. This heat exchange between the cathode air and the solid structure of the tubular cell is limited yielding a considerable cold spot at the cell inlet and higher thermal gradients. Another reason for the lower thermal gradients of the Delta8 cell can be found in the steam reforming reactions.

Fig. 16 shows the methane molar fraction as a function of the absolute cell length. The endothermal reforming reactions (STR) entail almost constant solid temperatures for all the investigated
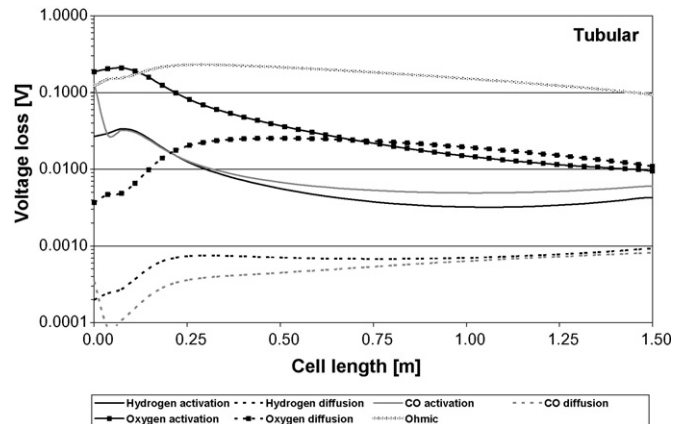
cell types until approximately 70% of the methane is converted. The planar cell exhibits an approximately six times lower catalyst load and the highest cell inlet temperature. In consequence, the STR is complete after 3 cm of the cell length. The tubular and the Delta8 cell have approximately the same catalyst load. Despite about 50 K higher inlet temperatures, the STR occurs slower in the Delta8 cell being complete after approximately 36 cm versus 30 cm for the tubular cell. The reasons for that are the more pronounced diffusion limitation due to the almost doubled hydraulic diameter of the anode channel and an approximately 30% higher catalyst load of the Delta8 cell compared to the tubular cell.

The local distribution of the voltage losses are depicted in Fig. 17 for the planar geometry, in Fig. 18 for the tubular geometry and in Fig. 19 for the Delta8 geometry, respectively. Note that the voltage losses are plotted is in logarithmic scale on the ordinate. For the planar geometry, diffusion losses are approximately two to three orders of magnitude lower than all other voltage losses. This is due to the very short diffusion path length of the investigated electrolyte supported cell micro geometry. Concerning the anode activation losses, the planar cell differs significantly from the tubular and Delta8 cell. In the front parts of the planar cell, anode and cathode activation losses are on comparable level with the ohmic losses. Towards the cell end the cathode activation and the ohmic losses decrease strongly yielding values about one order of magnitude smaller than the anode activation losses. This can be explained by the high prevalent temperature at the cell outlet which induces high conductivity of the YSZ electrolyte. The decreasing anode product partial pressures towards the cell end, due to fuel deple-
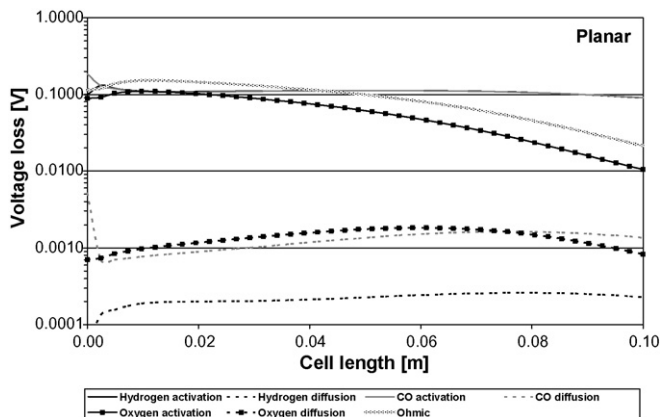

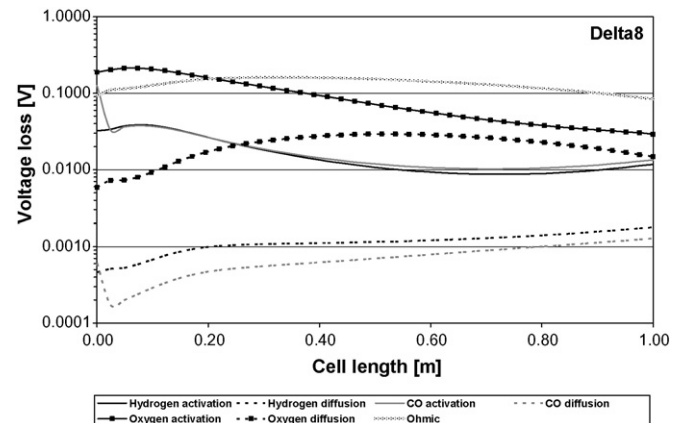Fig. 17. Voltage loss distribution of planar cell.

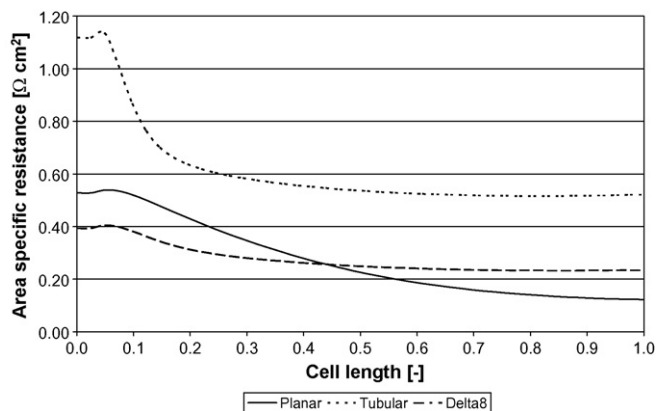Fig. 19. Voltage loss distribution of Delta8 cell.

Fig. 20. Area specific resistance distribution of planar, tubular and Delta8 cell.

tion, in contrast inhibit such a decrease for the anode activation losses. This phenomenon can neither be observed for the tubular nor for the Delta8 cell, indicating that the employed model parameters characterize an electrochemically very active anode catalyst used in these cells which allows electrochemical conversion with very low voltage losses even at low educt partial pressures. As a result of the assumption that the tubular and the Delta8 cell feature the same anode and cathode electrode material, the voltage loss pattern of both cells is quite similar. Anodic diffusion losses are negligible as is also the case for the planar cell design. In the cell regions where the steam reforming reactions cause very low solid temperatures, the cathode activation losses are higher than the ohmic losses. The picture changes however after completion of the reforming reactions with the associated strong temperature increase. In case of the tubular cell, the cathode activation losses decrease to values even lower than the cathode diffusion losses. A similar trend can be observed for the Delta8 cell. However, the thinner cathode electrode of the Delta8 geometry inhibits the diffusion losses to be come higher than the cathode activation losses.

The ohmic losses are very important for all three investigated cell designs. Ohmic losses are straightforwardly computed via the prevalent current density and the area specific resistance. The area specific resistance depends on the temperature-dependent ionic and electronic conductivity and the geometry of the current conducting parts of the cells. The calculation was discussed in detail before. Fig. 20 shows the area specific ohmic resistance (ASR) of the three investigated cells plotted vs. the dimensionless cell length. The tubular cell features the highest ASR due to the longest current path with approximately 31 mm. Further, the tubular cell ASR is strongly linked to the prevalent solid temperature due to the employed YSZ electrolyte. In the cold cell inlet region where the cell temperature is about 1000 K, the ionic conductivity of the YSZ electrolyte is only one tenth of value corresponding to the mean cell temperature of 1273 K. The strong temperature increase after completion of the steam reforming reactions explains the steep decrease of the ASR of the tubular cell. The Delta8 cell in contrast shows only a slight decrease of the ASR despite that the local cell temperatures increase from 1050 K at the cell inlet to 1300 K at the cell outlet. The reason for this is that the dominating role of the electrolyte for the ASR is weakened by the employed ScSZ electrolyte material. The rest of the employed conducting materials, namely the electrode and interconnect materials, are not as sensitive towards the local temperature. Despite that the Delta8 cell features a ScSZ electrolyte with approximately one third of the specific resistance of the YSZ electrolyte and a 20% shorter current path length, the corresponding ASR is in average only 50% lower than that of the tubular cell. The reason for that can be found in the 30% thin-

ner cathode electrode of the Delta8 cell and the according reduction of the current conducting cross-sectional area which compensates the shorter current path.

As expected, the ASR of the planar cell is significantly lower than that of the tubular cell due to its very short current path length of approximately 3 mm. However, the thick YSZ electrolyte induces a strong temperature dependency of the planar cell ASR which leads to higher values than the Delta8 cell at the cell inlet despite approximately 50 K higher solid temperatures. Comparing the Delta8 cell with the planar cell shows that in average the ASR of both cell designs is on a comparable level. That clearly demonstrates the improvements which were made in the development of the Delta8 cell compared to its predecessor, the standard tubular cell design.

5. Conclusions

A generalized, finite volume-based SOFC model has been developed. The model includes charge, mass and heat transport as well as a Langmuir–Hinshelwood type applied kinetics models for the steam reforming reaction. The model development was focused on a fast applicability to various cell geometries, short calculation times to allow for system analysis calculations and high fuel flexibility. The model was applied to a planar, the standard tubular and the triangular tube cell geometry (Delta8), showing good agreement with experimental and benchmark test data. Based on the computed local species, temperature, current density and voltage loss distributions, the performance of the three investigated cell designs was discussed, giving deep insight into the interrelations between cell geometry and transport phenomena inside the cells. It was shown that the performance of the tubular design was improved by introducing the Delta8 designs. The Delta8 design features a more homogeneous temperature distribution than the standard tubular cell due to improved heat exchange between cathode air and solid structure. This eliminates the strong cold spot at the cell inlet observed for the standard tubular cell. This, together with the employed ScSZ electrolyte, results in area specific resistance values of the Delta8 cell which are approximately half of the standard tubular values. In consequence, the performance of the new Delta8 cell design is almost double that of the standard tubular design. The planar electrolyte supported cell is also outperformed by the Delta8 cell. In future, our model will be included in a flow-sheeting software package allowing for detailed systems analysis calculations of SOFC-based power plants applying different fuels such as, e.g. biomass gasification derived producer gases, biogas, coal gas, etc.

References

[1] H. Kim, C. Lu, W.L. Worrell, J.M. Vohs, R.J. Gorte, J. Electrochem. Soc. 149 (2002) A247–A250.
[2] C. Stiller, B. Thorud, S. Seljebø, Ø. Mathisen, H. Karoliussen, O. Bolland, J. Power Sources 141 (2005) 227–240.
[3] F. Lange, M. Ise, W. Kleinlein, B. Schricker, Proceedings of the Fuel Cell Seminar & Exposition, San Antonio, USA, October 15–19, 2007.
[4] T. Kivisaari, P. Björnbom, C. Sylwan, B. Jacquinot, D. Jansen, A. de Groot, Chem. Eng. J. 100 (2004) 167–180.
[5] A.O. Omosun, A. Bauen, N.P. Brandon, C.S. Adjiman, D. Hart, J. Power Sources 121 (2004) 96–106.
[6] K.D. Panopoulos, L.E. Fryda, J. Karl, S. Poulou, E. Kakaras, J. Power Sources 159 (2006) 570–585.
[7] T. Proell, R. Rauch, C. Aichering, H. Hofbauer, Proceedings of the ASME Turbo Expo 2004: Power for Land, Sea and Air, Vienna, Austria June 14–17, 2004.
[8] W. Zhang, E. Croiset, P.L. Douglas, M.W. Fowler, E. Entchev, Energy Convers. Manage. 46 (2005) 181–196.
[9] R. Suwanwarangkul, E. Croiset, M.D. Pritzker, M.W. Fowler, P.L. Douglas, E. Entchev, J. Power Sources 166 (2007) 386–399.
[10] A. Selimovic, Modelling of solid oxide fuel cells applied to the analysis of integrated systems with gas turbines, Dissertation, Lund University, Lund, Sweden, 2002.

     F.P. Nagel et al. / Journal of Power Sources 184 (2008) 143–164

[11] C. Rechenauer, E. Achenbach, Dreidimensionale mathematische Modellierung des stationären und instationären Verhaltens oxidkeramischer Hochtemperatur-Brennstoffzellen, Dissertation, RWTH Aachen, Jülich, Germany, 1992.

[12] U. Bossel, Facts & Figures, Berne, Switzerland, 1992.

[13] S. Campanari, P. Iora, J. Power Sources 132 (2004) 113–126.

[14] S. Campanari, P. Iora, Fuel Cells 5 (2005) 34–51.

[15] Website, http://www.athenavisual.com, June 2007.

[16] B. Todd, J.B. Young, J. Power Sources 110 (2002) 186–200.

[17] F.A. Aly, L.L. Lee, Fluid Phase Equilib. 6 (1981) 169–179.

[18] Website, http://dippr.byu.edu/, December 2007.

[19] B.E. Poling, J.M. Prausnitz, J.P. O'Connell, The Properties of Gases and Liquids, McGraw-Hill Professional, New York, USA, 2000.

[20] E. Schmidt, Einführung in die technische Thermodynamik, Springer, Berlin/Göttingen/Heidelberg, Germany, 1963.

[21] J.M. Bockris, S. Srinivasan, Fuel cells: Their Electrochemistry, McGraw-Hill, New York, USA, 1969.

[22] P. Costamagna, K. Honegger, J. Electrochem. Soc. 145 (1998) 3995–4007.

[23] N.Q. Minh, T. Takahashi, Science and Technology of Ceramic Fuel Cells, Elsevier Science, Amsterdam, The Netherlands, 1995.

[24] E. Hernández-Pacheco, D. Singh, P.N. Hutton, N. Patel, M.D. Mann, J. Power Sources 138 (2004) 174–186.

[25] K. Nisancioglu, Proceedings of the Workshop on Mathematical Modelling: "Natural gas Fuelled Solide Oxide Fuel Cells and Systems", Charmey, Switzerland, July 2–6, 1989.

[26] E.F. Sverdrup, C.J. Warde, R.L. Eback, Energy Convers. 13 (1973) 129–141.

[27] A. Solheim, K. Nisancioglu, Proceedings of the Second International Symposium on SOFC, Greece, Athens, July 2–5, 1991.

[28] B. Thorud, Dynamic modelling and characterisation of a solid oxide fuel cell integrated in a gas turbine cycle, Dissertation, Norwegian University of Science and Technology, Trondheim, Norway, 2005.

[29] N.P. Cheremisinoff, Handbook of Heat and Mass Transfer, Butterworth-Heinemann, Houston/London/Paris, 1986.

[30] I. Drescher, Kinetik der Methan-Dampf-Reformierung, Dissertation, Forschungszentrum, Jülich, Jülich, Germany, 1999.

[31] C. Stiller, Design, Operation and control modelling of SOFC/GT hybrid systems, Dissertation, Norwegian University of Science and Technology, Trondheim, Norway, 2006.

[32] M. Pfafferodt, P. Heidebrecht, M. Stelter, K. Sundmacher, J. Power Sources 149 (2005) 53–62.

[33] P. Costamagna, E. Arato, P.L. Antonucci, V. Antonucci, Chem. Eng. Sci. 51 (1996) 3013–3018.

[34] E. Achenbach, Annex II: modelling and evaluation of advanced solid oxide fuel cells, IEA Programme on R&D on Advanced Fuel Cells: Final Report of Activity A2, Forschungszentrum Jülich, Germany, 1996.

[35] S.C. Singhal, K. Kendall, High-temperature Solid Oxide Fuel Cells: Fundamentals, Design and Applications, Elsevier, London, Great Britain, 2004.

[36] S.M. Haile, Acta Mater. 51 (2003) 5981–6000.

[37] K. Huang, Proceedings of the Fuel Cell Seminar & Exposition, San Antonio, USA, October 15–19, 2007.